

REPLY

M. Fassin · D. Kowollik · S. Wulfinghoff · S. Reese ·
M. Haupt

Design studies of rocket engine cooling structures for fatigue experiments

Received: 22 May 2015 / Accepted: 23 June 2016 / Published online: 18 July 2016
© Springer-Verlag Berlin Heidelberg 2016

Abstract The fatigue life of a regeneratively cooled rocket engine is strongly controlled by the aerothermodynamic cyclic load of the combustion chamber structure. Experiments on a subscale rectangular rocket combustion chamber operated with gaseous methane (GCH₄) are designed in order to investigate the structural response of the combustion chamber and the failure phenomena. Several design studies of the cooling channel structure of a replaceable fatigue specimen are presented, first based on one-cycle computations, later based on the computation of 20 cycles. One important aim of the work is to identify appropriate cooling channel structures and boundary conditions such that failure occurs after a relatively small number of cycles and in the centre cooling channels. The idea is to use the designed experiments for the validation of damage models in combination with fluid–structure interaction analysis.

Keywords Viscoplasticity · Damage · Thrust chamber · Thermomechanical coupling · Finite element simulation

1 Introduction

Precise knowledge of the coupled heat transfer processes in rocket engines is mandatory since the high temperature differences between the hot combustion gases and the cooling fluid lead to high heat transfer coefficients, resulting in heat flux levels up to 131–147 MW/m² acting at the throat region (see Quentmeyer [1]) on the combustion chamber cooling channel structure. The thin-wall structure is in general cooled by the cryogenic fuel. The resulting thermal gradient through the wall is in the range of 380–430 K/mm near the nozzle throat. During one cycle, the typical 1-mm-thin cooling channel wall is subjected to transient thermomechanical loads due to a pre-cooling, hot run and post-cooling phase. These cyclic loads induce the accumulation of plastic deformation and finally lead to failure. Since the deformed shape of the cooling channel wall after failure resembles the shape of a doghouse, the failure mode is called doghouse effect (see Riccius et al. [2]). In this deformation mode, the cooling channel wall becomes thinner and bulges towards the interior of the chamber. The failure can be related rather to ductile rupture than to low-cycle fatigue, see, for example, Schwarz et al. [3] for CuAgZr. In general, for low-cycle fatigue the number of cycles up to failure lies between 10² and 10⁴ (see, for example, Dufailly and Lemaitre [4]). Dufailly and Lemaitre [4] show that for a very low number of cycles to failure, the so-called Coffin–Manson law (which relates the number of cycles to failure to the plastic strain

M. Fassin (✉) · S. Wulfinghoff · S. Reese
Institute of Applied Mechanics, RWTH Aachen University, 52074 Aachen, Germany
E-mail: marek.fassin@rwth-aachen.de

D. Kowollik · M. Haupt
Institute of Aircraft Design and Lightweight Structures, Technische Universität Braunschweig, 38108 Brunswick, Germany

rate amplitude) overpredicts the realistic number of cycles to failure. For this reason, Dufailly and Lemaitre suggest the wording “very low cycle fatigue” for the cases where the number of cycles to failure is of the order ten. They propose for the case of “very low cycle fatigue” a ductile damage model which is very similar to the model used in the present paper.

An experimental database of the complex heat transfer processes and the structural response of cooled rocket engines is essential for the validation of numerical tools. The importance of these data is confirmed by the fact that life cycle prediction of rocket engines strongly depends on the accuracy of wall temperature predictions. This is due to the strong temperature dependency of the copper material at elevated temperatures. Fröhlich et al. [5] and Immich et al. [6] mention that lifetime prediction with a temperature error of 40 K might lead to 50 % lifetime reduction in a cryogenic propellant rocket combustion chamber. Therefore, a carefully designed experiment is needed to improve the temperature prediction and analyse the doghouse effect.

Many fatigue life experiments on combustion chamber structures were conducted in the past. Only a small part of this research has been published in the public domain. Quentmeyer was one of the first to systematically investigate the low-cycle fatigue of a cylindrical rocket thrust chamber, see Quentmeyer [1]. Twenty-one thrust chambers were manufactured out of three different alloys and cycled to failure. The instrumentation consisted of thermocouples placed into the cooling channel rib. In addition to this, thermocouples were placed in the inlet and outlet manifold of the cooling fluid. Therefore, the inlet and outlet temperatures were not measured for individual cooling channels. Also the deformation of the hot gas wall remained unknown, between cycles as well as at failure. For the entire coolant supply system, a fixed upstream and downstream valve position was used, being dependent on the decreasing coolant tank pressure and temperature. For the chosen cooling channel geometry and most of the investigated alloys, hundreds of cycles were necessary until failure occurred.

Anderson designed and investigated a water-cooled subscale round combustion chamber with the focus on lifetime analyses, see Anderson et al. [7]. The deformation was measured between cycles, through disassembling the entire fatigue segment. An unexpected type of failure occurred near the 100th cycle. The rear stainless steel jacket of the cooling channel was not bonded to the copper cooling channel structure. Anderson assumes that the gap increased during the cycles, which might have changed the cooling efficiency of the structure. No individual control and instrumentation of the cooling channel fluid flow was carried out. Neither in [1] nor in [7] efforts were made to reduce the number of cycles leading to failure. This is, however, important to reduce the consumption of resources such as fuel, oxidizer and cooling gas. For this reason, in the present work, we strive for a design which allows us to study fatigue after a quite small number of cycles.

In Riccius et al. [8], cyclic laser heating (as replacement for the hot gas) was applied to an actively cooled small section of the hot gas wall, called thermomechanical fatigue (TMF) panel. With the laser device, heat fluxes up to 20 MW/m² were possible. Via infrared camera, the temperature field on the surface of the laser-heated side of the TMF panel could be measured. Together with the measurement of temperature, pressure and mass flow rate of the coolant, data for the combined validation of the CFD analysis of the coolant flow and the thermal analysis of the wall structure were available internally at DLR. A stereo camera system was used for the measurement of the deformation field of the laser-heated side during hot run and cooling phases. This, together with the above-mentioned measurements, provided data for the conducted validation of the structural analysis of the thermally loaded structure. Riccius et al. worked with an elastoplastic material model according to the rate-independent version of the Chaboche model [9,10]. For fatigue life estimation, a post-processing method using Coffin–Manson’s law (use of the so-called usage factors) was applied. The calculated number of cycles to failure was underestimated by about 32 % compared with experimental results.

Within the field of computational structural mechanics, research on the investigation of the doghouse effect by using finite element modelling started in the early 1990s. Arya [11] presented first FE computations of a cylindrical rocket nozzle model applying three different viscoplastic material models. In [12], Arya and Arnold employed Robinsons’ unified viscoplastic material model for an extensive stress and strain analysis of an experimental cylindrical thrust chamber. Butler et al. [13] used the cylindrical version of the higher-order theory for functionally graded materials and compared two inelastic models for the liner’s material, namely Robinsons’ unified viscoplastic model and the power-law creep model. Comparison of the results showed that the latter one predicts the experimentally observed deformation more precisely.

The fatigue life of a thrust cell liner is affected by various factors. Riccius et al. discussed in [14] the geometry optimization of cryogenic liquid rocket combustion chambers. In Riccius et al. [15], a comparative study of using either stationary or dynamic thermal analyses was presented. Additionally, rate-independent and rate-dependent structural analyses were compared. Riccius et al. [15] did not include damage in their material model. Instead, a post-processing approach was utilized for fatigue life estimation. Furthermore, all

computations were restricted to 2D. For the comparison of 2D and 3D structural FE analyses, see Riccius et al. [16].

Schwarz et al. [3] developed a viscoplastic material model coupled with anisotropic damage, represented by a second-order tensor. In the proposed model also micro-defect closure effects and material ageing were taken into account. Schwarz et al. [17] compared the damage distribution and the number of cycles up to failure for two different damage modelling concepts—(1) an anisotropic damage model and (2) an isotropic damage model, both with and without including micro-defect closure effects. They concluded that neither damage anisotropy nor micro-defect closure effects strongly affect the global failure phenomenology. But, it was found that the typically observed excessive bulging and thinning of the hot gas wall are decreased if damage anisotropy and micro-defect closure effects are not taken into account. For the purpose of determining the location of failure as well as the number of cycles up to failure also the less complex models (isotropic damage and no micro-defect closure effects) yield sufficiently precise results.

For the presented design studies in this paper—aiming mainly at the estimation of the qualitative behaviour of the fatigue specimen—a less complex model is preferable. The applied material model is based on the classical Armstrong–Frederick kinematic hardening model, which is extended to include rate dependence of Perzyna-type [18] and Lemaitre-type ductile damage (see, for example, Lemaitre [19]). For a detailed description of the model, see Kowollik et al. [20], where the model was already utilized for a thermomechanical analysis of a combustion chamber segment and could be shown to qualitatively reproduce the doghouse effect.

To the knowledge of the authors, a rectangular combustor with replaceable fatigue specimen has not been investigated so far. This novel approach enables the investigation of several fatigue specimens under equal boundary conditions. A cooled inspection plate on the opposite side allows to inspect and measure the structural deformation and the roughness increase between test cycles without changing the mechanical boundary conditions of the fatigue specimen.

The focus of this work is on the investigation of the key processes leading to the wall damage of a cooled combustion chamber. To achieve this goal with quantitative measurements, a previously developed damage model is utilized during the design phase of a replaceable fatigue specimen. This specimen is planned to be mounted to a fatigue test segment of a modular subscale combustion chamber which is currently under development. The aim of the fatigue analysis is to identify cooling channel structures and suitable boundary conditions that lead to failure after a few engine cycles at the point of interest, where detailed quantitative measurements can be taken. The overall goal is to develop an experiment which provides valuable quantitative data for the validation of damage modelling in combination with fluid–structure interaction. The important interactions to be analysed are, for example, (1) the thermal interaction, where the hot gas heat flux response is influenced by the structural thermal behaviour and the cooling fluid heat flux response, (2) the mechanical interaction, where in addition to the thermal expansion the pressure difference between hot gas and cooling fluid results in a cooling channel wall deformation, and (3) the chemical interaction, where the hot gas can react with the surface and generates a roughness increase resulting in more friction and higher heat flux. Moreover, an interaction between several of these mechanisms occurs, where the roughness increase generates a higher heat flux and influences the structural temperature response and consequently the wall deformation. The increased wall deformation alters the hot gas flow and may lead to a higher heat flux.

For the purpose of validation, a multi-injector combustion chamber has been designed for gaseous oxygen (GOX) and gaseous methane (GCH₄). The chamber provides well-defined boundary conditions. A step-by-step development of the combustion chamber hardware and set-up is mandatory to increase complexity such as injector design, propellant mixing and combustion characteristics in a reasonable manner. A first experimental investigation of a single-injector hardware with identical injector dimensions and contraction ratio as the planned final hardware of a quasi-2D 5-injector combustor was published by Celano et al. in [21].

The present article is organised as follows: in Sect. 2, the problem is defined in detail through the comparison between a full-scale rocket engine and the rectangular subscale rocket engine, whose experimental environment is presented. The previously developed damage model to analyse the mechanical response of the fatigue specimen's cooling structure is presented in Sect. 3. Section 4 is devoted to the description and approximation of the thermal boundary conditions. Moreover, the influence of the cooling channel geometry and the boundary conditions on the cooling fluid system is analysed and discussed. The design studies for doghouse failure are presented and discussed in detail in Sect. 5. The resultant conclusions from Sect. 5 are incorporated in the design of the entire fatigue test segment. A short design outlook of the fatigue segment is given in Sect. 6. Section 7 summarizes the drawn conclusions and gives an outlook towards further steps.

2 Problem definition

The main advantage of a subscale test lies in lower manufacturing costs and much lower resources needed to operate the engine. The present work focuses on the analysis of fatigue. Multiple combustion chambers need to be manufactured and tested up to failure in order to gain a necessary database. The application of several measurement techniques and regulators to control cooling fluid flow is limited due to the small dimensions of a typical cylindrical subscale chamber. An innovative modular rectangular subscale chamber design is under development in order to analyse fatigue for a specimen mounted to a reusable fatigue test segment. The rectangular design allows simple access to the specimen surface through the opposite wall. The flat specimen provides the possibility to be able to design cooling channels with wide fins in order to measure the temperature response inside the cooling channel fin near the hot gas surface. Several different measuring techniques shall be used, e.g. multiple thermocouples in the cooling channel fins, optical scanning of hot gas surface deformation and individual cooling channel temperature and pressure measurement in combination with mass flow rate regulation. These new options allow to generate a valuable database to validate several numerical approaches with different analysing depth, e.g. fully three-dimensional coupling approaches including a damage model.

On the subscale level, the specimen of the rectangular chamber is designed to meet a similar pressure difference between hot gas and cooling fluid as well as the maximum hot gas wall temperature of a full-scale engine. These parameters shall be varied in order to analyse their effect on the lifetime of the specimen. In the following, a typical full-scale liquid rocket combustion chamber and the planned rectangular subscale gaseous combustion chamber are described and compared.

2.1 Full-scale application: a liquid rocket combustion chamber

In Fig. 1 (left), a typical rocket combustion chamber is shown. As shown in the schematic cross section in the middle of Fig. 1, the rocket combustion chamber wall consists of copper liners and a nickel jacket. Usually, there is a huge number of cooling channels, e.g. 360, for the whole cylindrical cross section. Schematically, only 5 cooling channels are depicted, to show the general configuration. Due to rotational symmetry, a model can be derived with a segment of one half of a cooling channel (right-hand side of Fig. 1). Mechanical as well as thermal boundary conditions are given through symmetry conditions on the cutting planes.

2.2 Subscale test: modular rectangular GOX/GCH4 combustion chamber

For the subscale investigations, the experimental configuration is simplified to a nearly two-dimensional system realised by a rectangular combustion chamber. It will be driven by gaseous oxygen (GOX) and gaseous methane (GCH4). The rectangular configuration lowers the manufacturing costs compared to an entire cylindrical specimen segment and simplifies the numerical modelling. The modular concept shown in Fig. 2 allows to analyse different aspects of the physical phenomena involved, e.g. combustion efficiency, such as injector design, injector wall interaction and characteristic chamber length (defined as the ratio between chamber

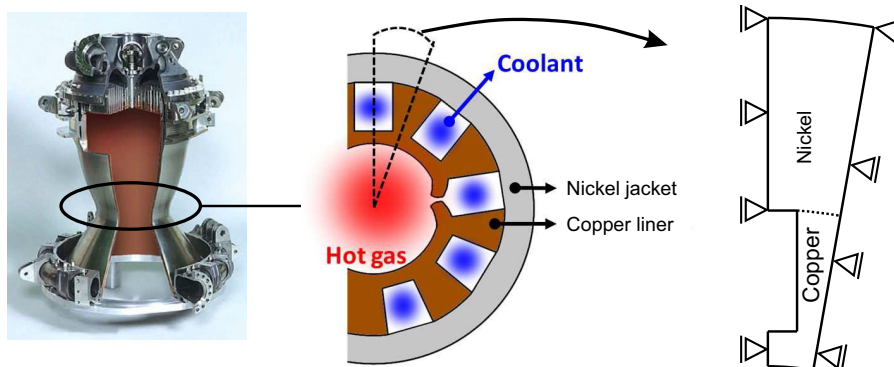


Fig. 1 A typical rocket combustion chamber [22] (left); its schematic cross section (middle); the segment of one half of a cooling channel (right)

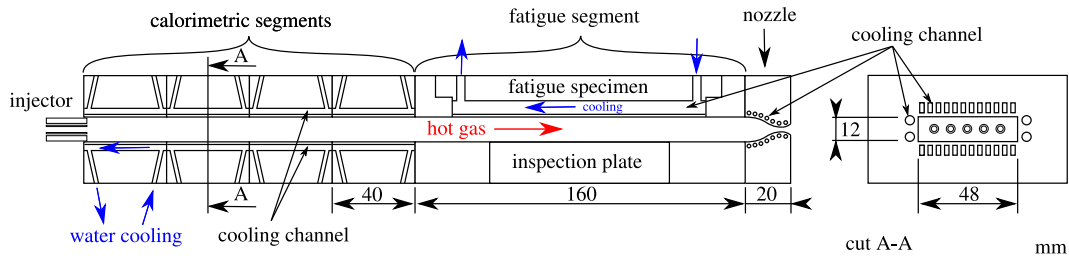


Fig. 2 Sketch of the subscale combustion chamber

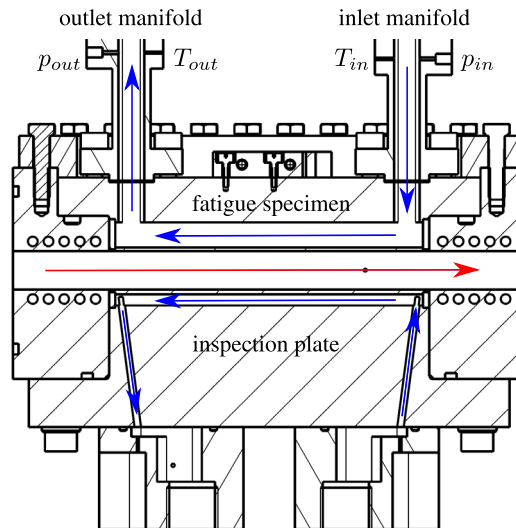


Fig. 3 Cut view of the fatigue segment assembly with an actively cooled inspection plate opposite of the fatigue specimen (arrows indicate hot gas and cold fluid flow directions)

volume and throat cross section area), or fatigue of the chamber wall. The experimental set-up consists of an injector segment with five coaxial injectors, multiple 40-mm calorimetric segments, the 160-mm fatigue segment and a 20-mm small nozzle segment which is needed to generate a supersonic outflow. The cut view A–A shows the cross section dimensions (width 48 mm; height 12 mm). The calorimetric segments and the nozzle segment are completely water-cooled below 600 K in order to guarantee a long chamber life.

The purpose of the independent fatigue segment shown in detail in Fig. 3 is the possibility to frame a replaceable flat fatigue specimen to analyse the fluid–structure interaction and the lifetime of the cooling channel structures. In addition to the wall deformation towards the chamber, it is expected that a roughness increase at elevated temperatures occurs throughout the test cycles, see Kiesner et al. [23]. These structural changes have an impact on the hot gas heat flux response. The thermal response on the structural side might change the lifetime of the specimen significantly. Both aspects shall be investigated and measured throughout the planned test cycles.

The symmetric temperature distribution in the cross section is verified by temperature measurements using thermocouples in the cooling channel fin of the fatigue specimen at several positions of the cross section, see Fig. 4. In addition to this, the heat-up of the fatigue specimen is measured in chamber axis for one cooling channel fin. Furthermore, in each direction the temperature is measured in two different heights. These data are valuable to especially validate a thermal fluid–structure interaction analysis, where the hot gas, structure and cooling channel fluid flow interact with each other.

To enable access to optical and contact measurement techniques between test cycles, an inspection plate is built into the opposite wall. Cross-cooling channels are placed at the beginning and at the end of the fatigue segment. The dismounting of the inspection plate gives simple access to the specimen surface and enables a measurement of the cooling channel wall deformation between the test cycles. A laser sheet scanner is used to measure deformation profiles normal to the hot gas wall. Therefore, the specimen with all of the attached

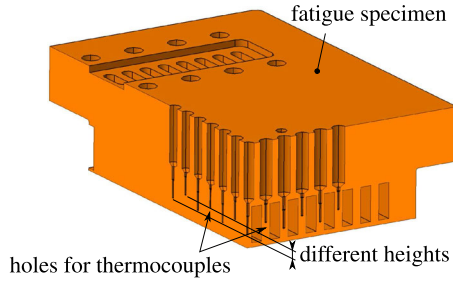


Fig. 4 Temperature measurement of fatigue specimen in two directions and different heights

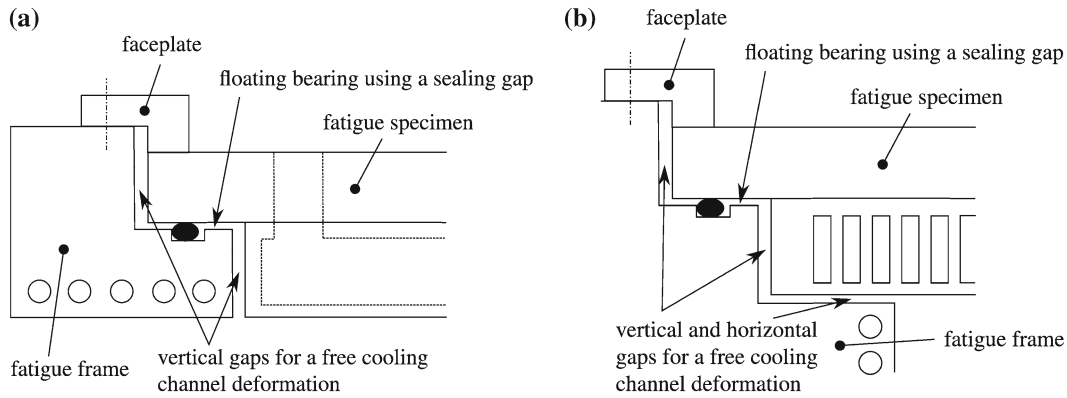


Fig. 5 Illustration of the floating bearing of the fatigue specimen. **a** Bearing in longitudinal cooling channel direction. **b** Transverse cooling channel bearing

Table 1 Combustion and cooling operation in one cycle

Phase (-)	Time (s)	Combustion (-)	Cooling (-)
Pre-cooling	0-2	Off	On
Hot run	2-22	On	On
Post-cooling	22-40	Off	On

sensors and cooling manifolds does not need to be disjoined between test cycles. In addition to this, it is planned to measure the roughness increase throughout the test cycles.

For the numerical simulation, well-defined mechanical boundary conditions of the specimen are essential. Figure 5 shows an option: a floating bearing. Vertical gaps allow a free in-plane deformation of the specimen. The floating bearing is realised through a small horizontal gap, which contains the sealing. A separate faceplate is used to provide a uniform clamping between the fatigue specimen and the fatigue segment. The design studies described in Sect. 5 will show the influence of the specimen boundary conditions on the desired fatigue behaviour. The target is a bulging cooling channel structure with a maximum deformation and failure in the centre of the specimen.

2.3 Cooling of fatigue specimen

The loading cycle applied to the subscale combustion chamber consists of three phases: pre-cooling, hot run and post-cooling. The combustion and cooling operation for the individual phases are summarized in Table 1 (for the bulk temperatures and heat transfer coefficients, see Table 9 in Sect. 5.1). The cooling of the specimen is realised with a gaseous nitrogen cooling system, schematically shown in Fig. 6. A gas tank (with 30 MPa) is blown down against the atmosphere during the test cycles. The coolant flow through the specimen and its manifolds is shown by arrows in Fig. 7. For appropriate validation conditions, the coolant flow is carefully measured and controlled. The inlet flow is pressure-controlled in a closed loop for the entire number of cooling channels. A perpendicular inlet with a comparatively large chamber is used to provide an evenly distributed

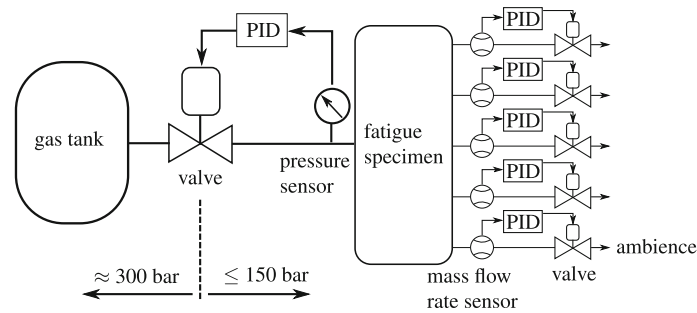


Fig. 6 Sketch of the cooling system of the fatigue specimen (PID: proportional–integral–derivative controller)

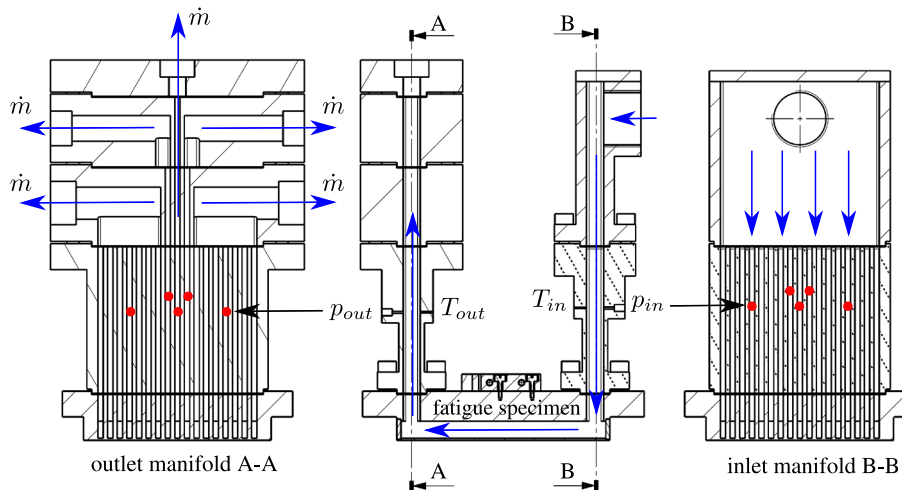


Fig. 7 Fatigue specimen and manifold design. Positions of thermocouples and pressure transducers are given in red dots

inlet condition for the cooling channels. The closed loop mass flow rate control is realised individually for the three centre cooling channels. The outside cooling channels are combined into two outlets, whereas each mass flow rate is separately controlled in a closed loop, see the outlet manifold in Fig. 7. Herewith a symmetric cooling is established especially for the three centre channels of the fatigue specimen, which are the area of interest for validation. In addition, pressure and temperature are measured in the vicinity of the inlet and outlet of the specimen cooling channels, see positions in Fig. 7. These data are used to compute the enthalpy increase of the cooling channel and completes the validation database.

2.4 Fatigue specimen

Since there are no available data for the design of rectangular combustion chambers in the literature, it is necessary to develop appropriate thermal and mechanical boundary conditions and the specimen geometry to obtain meaningful experimental results about the fatigue behaviour. Identifying such configurations leading to failure after a few engine cycles at the point of interest is the key issue of this work and is described in the next chapters. These studies will finally define the specimen boundary conditions and geometry (Fig. 8), i.e. the number of cooling channels, their length l , height h and width b as well as the thicknesses of the hot gas wall t_{hg} , of the fin b_f and of the rear wall.

2.5 Comparison between the rectangular subscale rocket thrust chamber and the full-scale application

The experimental conditions and configuration of the fatigue specimen are chosen such that they are similar to real nozzle conditions, i.e. individual cooling channels with appropriate pressure and mass flow rate to reach a realistic temperature level. Nevertheless, there are significant discrepancies between the full-scale

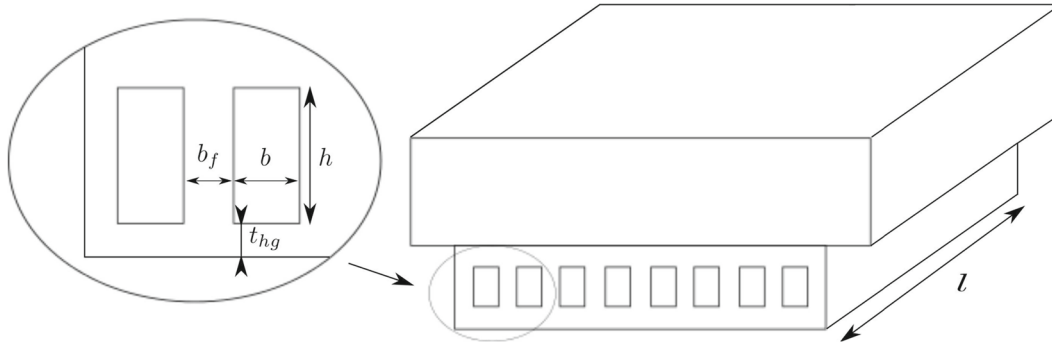


Fig. 8 Sketch of the fatigue specimen

Table 2 Comparison of boundary conditions for the quasi-Vulcain thrust chamber and the fatigue specimen

Boundary condition	Quasi-Vulcain	Fatigue specimen
Coolant pressure p_{cf} (MPa)	15	7–14
Hot gas pressure p_{hg} (MPa)	10	2
Heat flux q_{hg} (MW/m ²)	120	≈7.4
Coolant temperature T_{cf} (K)	50	≈293
Heat transfer coefficient α_{cf} (kW/m ² K)	50	≈1.8–5.0

and the subscale combustion chamber boundary conditions, see Table 2. The subscale chamber is operated at 20 % combustion pressure compared to the full-scale engine. To generate a similar mechanical loading of the cooling channel structure, a pressure difference of 5 MPa between the hot gas and the coolant is desired. First, all computations are performed with $p_{cf} = 7$ MPa. In the end, the coolant pressure is increased to $p_{cf} = 14$ MPa (resulting in a pressure difference of 12 MPa) in order to study the influence of this load on the fatigue behaviour. The reduced chamber pressure and the location of the fatigue specimen inside the straight part of the chamber result in a heat flux level that is only 6 % compared to the nozzle throat region of the full-scale engine. This low heat flux level limits the achievable thermal gradient within the hot gas wall. Since the thermal gradient within the hot gas wall is smaller than in the full-scale application, at least the temperature level of the maximum occurring temperature should be similar. Carlile and Quentmeyer [24] state that for the occurrence of the doghouse effect, the lower temperature bound for T_{w1} is between 700 and 810 K. The maximum hot gas wall temperature $T_{w1} = 950$ K is selected as design point in order to promote an early failure after a small amount of engine cycles. During the experiment, the amount of load cycles to failure will be analysed by varying this temperature in the range of 800–950 K. For the full-scale engine, the hot run duration is about 600 s. The short hot run time of 20 s for the fatigue specimen was chosen because long cycles would require a tremendous amount of fuel and coolant. As the computations will show, damage is mainly increasing during heating up and cooling down, see Sect. 5. This is why the chosen short hot run is sufficient to cause damage in the hot gas wall. Despite the above-described differences between the full-scale and the subscale rocket thrust chamber, the subscale chamber offers good conditions to analyse the relevant fluid–structure interaction phenomena between hot gas, structure and cooling fluid flow. The studies below show also that the new experimental set-up is able to produce a failure similar to the doghouse failure mode.

3 Material modelling

3.1 Motivation by a rheological model

Starting point of our material modelling is the classical rheological model for elastoplasticity with Armstrong–Frederick kinematic hardening [25]. This rate-independent model is extended to a viscoplastic material model including isotropic damage (see rheological model in Fig. 9). Here σ_y represents the yield stress of the material and η is the viscosity parameter. By choosing appropriate values for the hardening spring E_h and the dimensionless parameter b , the nonlinear effect of kinematic hardening can be represented. In this context, the parameter $\eta_h = E_h/(\lambda b)$ is defined. The dotted lines of the front spring emphasize the degradation of the

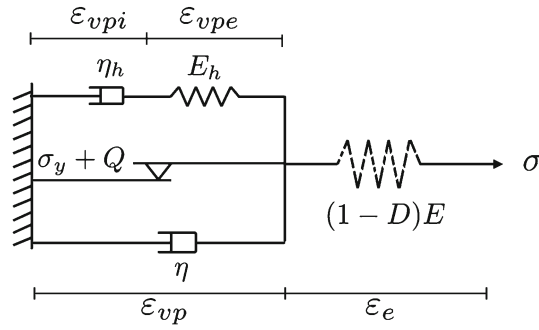


Fig. 9 Extension of the Armstrong–Frederick kinematic hardening model into a viscoplastic damage model (rheological model)

elastic stiffness by damage. In the simplest case, a scalar damage variable, first introduced by Kachanov [26], is used. The damaged elastic spring constant is then given by

$$\tilde{E} = E(1 - D), \quad (1)$$

where D is the scalar variable for isotropic damage. Following Lemaitre's principle of strain equivalence (see, for example, Lemaitre [19]), the effective stress takes the form

$$\tilde{\sigma} = \sigma / (1 - D), \quad (2)$$

where the so-called continuum mechanical stress is denoted by σ and the so-called effective stress is denoted by $\tilde{\sigma}$. This notation applies for tensorial quantities (see Sect. 3.2) analogously.

3.2 Continuum mechanical extension within a small strain formulation

Based on the rheological model in Fig. 9, the constitutive equations for the continuum mechanical viscoplastic damage model in three dimensions are now derived. Within the small strain regime, the total strain

$$\boldsymbol{\varepsilon} = \text{sym}(\nabla \mathbf{u}) = \boldsymbol{\varepsilon}_e + \boldsymbol{\varepsilon}_{vp} + \boldsymbol{\varepsilon}_{th} \quad (3)$$

is additively split into elastic ($\boldsymbol{\varepsilon}_e$), viscoplastic ($\boldsymbol{\varepsilon}_{vp}$) and thermal ($\boldsymbol{\varepsilon}_{th}$) parts with the latter one being defined by

$$\boldsymbol{\varepsilon}_{th} = \beta_s (T - T_{ref}) \mathbf{I}. \quad (4)$$

Here β_s is the thermal expansion coefficient of the material, T_{ref} the bulk temperature, and \mathbf{I} the second-order identity tensor. For linear isotropic elasticity, the stress–strain relationship for the Lemaitre damage model [19] reads

$$\boldsymbol{\sigma} = \tilde{\mathbb{C}}[\boldsymbol{\varepsilon}_e] = \tilde{\mathbb{C}}[\boldsymbol{\varepsilon} - \boldsymbol{\varepsilon}_{vp} - \boldsymbol{\varepsilon}_{th}], \quad (5)$$

$$\tilde{\mathbb{C}} = (1 - D) \mathbb{C}, \quad (6)$$

where \mathbb{C} is the isotropic fourth-order elasticity tensor defined by the elastic modulus E and the Poisson's ratio ν . For the viscoplastic strain $\boldsymbol{\varepsilon}_{vp}$, a further decomposition into $\boldsymbol{\varepsilon}_{vpe}$ and $\boldsymbol{\varepsilon}_{vpi}$ is applied:

$$\boldsymbol{\varepsilon}_{vp} = \boldsymbol{\varepsilon}_{vpe} + \boldsymbol{\varepsilon}_{vpi}. \quad (7)$$

According to Lion [27], $\boldsymbol{\varepsilon}_{vpe}$ can be interpreted as an elastic strain on the micro-scale due to dislocation-induced lattice deformations. The strain $\boldsymbol{\varepsilon}_{vpi}$ can be interpreted in terms of the average of local inelastic slips on the micro-scale and is determined by an evolution law which will be shown later. The back stress deviator tensor \mathbf{X}^D [$(\cdot)^D$ represents the deviatoric term of a tensor] is then defined as

$$\mathbf{X}^D = 2\mu_{th} [\boldsymbol{\varepsilon}_{vpe}^D], \quad (8)$$

with μ_h denoting the shear modulus of the hardening part of the model. Applying J_2 flow theory with kinematic and isotropic hardening, the yield function takes the von Mises form

$$\Phi = \|\tilde{\sigma}^D - X^D\| - \sqrt{\frac{2}{3}} (\sigma_y + Q), \quad (9)$$

where $\|\cdot\|$ represents the L_2 norm of a tensor. The isotropic hardening function Q can be chosen in different ways. Here the saturation-type isotropic hardening rule of Voce [28]

$$Q = Q_0 (1 - \exp(-\kappa\alpha)), \quad (10)$$

is applied, with α being the state variable for isotropic hardening and Q_0 and κ the corresponding material parameters. The constitutive model contains three internal variables: the viscoplastic strain ϵ_{vp} , the (local inelastic) viscoplastic strain ϵ_{vpi} and the scalar damage variable D . The evolution equations of these internal variables are given as follows:

$$\dot{\epsilon}_{vp} = \dot{\lambda} \frac{\partial \Phi}{\partial \sigma} = \frac{\dot{\lambda}}{1 - D} \frac{\tilde{\sigma}^D - X^D}{\|\tilde{\sigma}^D - X^D\|}, \quad (11)$$

$$\dot{\epsilon}_{vpi} = \dot{\lambda} b \epsilon_{vpe}^D, \quad (12)$$

$$\dot{D} = \dot{p} \left(\frac{Y}{S}\right)^k H_{(p-p_D)}. \quad (13)$$

The evolution equation for the scalar damage variable D (see Eq. 13) is taken from Lemaitre [19] which is the same as Dufailly and Lemaitre [4] propose for “very low cycle fatigue”. This evolution equation accounts for multi-axial stress states, whereas the Coffin–Manson relation (low-cycle fatigue) is still limited in its application to uniaxial periodic loadings, see Dufailly and Lemaitre [4]. Furthermore, Dufailly and Lemaitre [4] show that in contrast to the Coffin–Manson relation, the number of cycles to failure is a function not only of the strain, but also of the stress amplitudes. The viscoplastic damage model is completed by the description of the plastic multiplier $\dot{\lambda}$ determined by

$$\dot{\lambda} = \frac{\langle \Phi \rangle^m}{\eta}. \quad (14)$$

For the calculation of the isotropic hardening function Q (cf. Eq. 10), the evolution of the isotropic hardening state variable α is needed which can be evaluated easily when $\dot{\lambda}$ is known and is given by

$$\dot{\alpha} = \sqrt{\frac{2}{3}} \dot{\lambda}. \quad (15)$$

Equation 13 describes the evolution of the scalar damage variable according to Lemaitre [19]. On the one hand, damage evolution is coupled to the accumulated viscoplastic strain rate defined by

$$\dot{p} = \sqrt{\frac{2}{3}} \|\dot{\epsilon}_{vp}\| = \sqrt{\frac{2}{3}} \frac{\dot{\lambda}}{1 - D}. \quad (16)$$

On the other hand, Y is denoting the energy released by loss of stiffness (cf. Lemaitre [19]) and is given by

$$Y = \frac{1}{2} \epsilon_c \cdot C [\epsilon_c] \quad (17)$$

which influences the growth of damage. The parameter p_D is the damage threshold determining the onset of damage. H is a step function, which is zero for $p < p_D$ and is equal to one for $p \geq p_D$. Furthermore, the material parameters S (energy strength of damage) and the exponent k occur in Eq. 13. For the calculation of the plastic multiplier $\dot{\lambda}$ (see Eq. 14), the Perzyna form (cf. [18]) is used. Therein η represents the viscosity parameter and m an additional parameter which allows a better fitting to experimental data. The symbol $\langle \cdot \rangle$ defines the Macaulay brackets, i.e. $\langle x \rangle = \frac{x+|x|}{2}$. The yield function Φ is normalized according to

$$\bar{\Phi} = \frac{\|\tilde{\sigma}^D - X^D\|}{\sqrt{\frac{2}{3}} (\sigma_y + Q)} - 1. \quad (18)$$

Table 3 Summary of the constitutive equations of the viscoplastic damage model

Effective elasticity tensor	$\tilde{\mathbb{C}} = (1 - D) \mathbb{C}$
Stress	$\boldsymbol{\sigma} = \tilde{\mathbb{C}} [\boldsymbol{\varepsilon}_e]$
Effective stress	$\tilde{\boldsymbol{\sigma}} = \mathbb{C} [\boldsymbol{\varepsilon}_e]$
Back stress deviator	$\mathbf{X}^D = 2\mu_h [\boldsymbol{\varepsilon}_{vpe}^D]$
Total strain	$\boldsymbol{\varepsilon} = \boldsymbol{\varepsilon}_e + \boldsymbol{\varepsilon}_{vp} + \boldsymbol{\varepsilon}_{th}$
Viscoplastic strain	$\boldsymbol{\varepsilon}_{vp} = \boldsymbol{\varepsilon}_{vpe} + \boldsymbol{\varepsilon}_{vpi}$
Yield function	$\Phi = \ \tilde{\boldsymbol{\sigma}}^D - \mathbf{X}^D\ - \sqrt{\frac{2}{3}} (\sigma_y + Q)$
Viscoplastic strain rate	$\dot{\boldsymbol{\varepsilon}}_{vp} = \frac{\dot{\lambda}}{1 - D} \frac{\tilde{\boldsymbol{\sigma}}^D - \mathbf{X}^D}{\ \tilde{\boldsymbol{\sigma}}^D - \mathbf{X}^D\ }$
(Local inelastic) viscoplastic strain rate	$\dot{\boldsymbol{\varepsilon}}_{vpi} = \dot{\lambda} b \boldsymbol{\varepsilon}_{vpe}^D$
Damage	$\dot{D} = \dot{p} \left(\frac{Y}{S}\right)^k H_{(p-p_D)}$
Plastic multiplier	$\dot{\lambda} = \frac{(\Phi)^m}{\eta}$

Table 4 Values of the yield stress and kinematic hardening parameters for a generic copper alloy [20]

σ_y (MPa)	E (GPa)	μ_h (MPa)	b (-)	T (K)
232	148	779.35	16.33	0
121	90	64.68	16.33	800
108	82	12.93	16.33	900
53	53	12.93	16.33	1300

In total, the model contains 11 temperature-dependent parameters: E and ν for the elastic behaviour, σ_y as yield stress, μ_h and b for the kinematic hardening, Q_0 and κ for isotropic hardening, S , k and p_D for damage and finally η and m for the viscous behaviour. A summary of the constitutive equations is given in Table 3.

3.3 Material parameters

For the thermomechanical analysis to be discussed in Sect. 5, the parameters for the material model introduced in the previous section have to be defined. The common material used for the full-scale application is CuAgZr. Since this material is very expensive, CuCr1Zr is investigated, a material expected to exhibit similar properties as CuAgZr, which is also used by DLR as rocket combustion chamber material for full-scale applications (see, for example, Riccius et al. [8] or Thiede et al. [29]). Since the experiments and the corresponding material parameter identification for CuCr1Zr is ongoing work, experimental data from the literature for a generic copper alloy are utilized for the design studies presented in this work. For the yield stress σ_y and Young's modulus E , data of a generic copper are adopted from Riccius and Zametaev [30]. For the kinematic hardening behaviour, data from Schwarz et al. [17] of a generic copper alloy are used. Schwarz et al. [17] describe the kinematic hardening by means of an evolution equation for the back stress \mathbf{X} instead of that for the (local inelastic) viscoplastic strain $\boldsymbol{\varepsilon}_{vpi}$ as it is done here. Therefore, the material parameters μ_h and b cannot be adopted directly, but have to be derived in an additional calculation. This is shown in detail in Kowollik et al. [20]. The Poisson's ratio ν is assumed to be equal to 0.34 and constant over temperature. Table 4 summarizes the values of the material parameters σ_y , E , μ_h and b for a generic copper alloy. For other temperatures, linear interpolation is carried out.

To illustrate the temperature dependency of the elastoplastic material parameters, strain-controlled uniaxial cyclic loadings (one cycle) neglecting damage and viscous effects are simulated at the gauss point level. Figure 10 shows the resulting stress–strain curves for five different temperatures.

The viscosity parameters η and m are adopted from experiments with CuCr1Zr (see Tini [31]). The values for the four evaluated temperatures are given in Table 5. For temperatures smaller than 293.15 K, the values for $T = 293.15$ K are valid. For temperatures larger than 873.15 K, the values for $T = 873.15$ K hold. Since neither experimental data nor suitable literature data for the damage parameters S , k and p_D are available, these parameters are chosen according to [20]. The damage threshold p_D is set equal to zero, meaning that damage

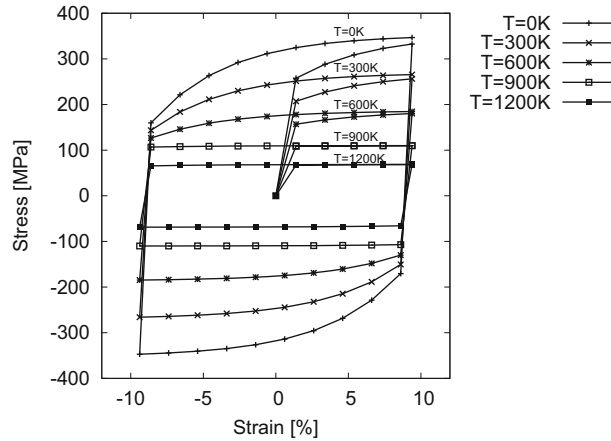


Fig. 10 Stress–strain curves of a generic copper alloy for one cycle neglecting damage and viscous effects [20]

Table 5 Temperature dependency of the viscous material parameters adopted from Tini [31]

T (K)	293.15	373.15	573.15	873.15
η (s)	0	0.07	2.0	18.0
m (-)	1	1	1	1

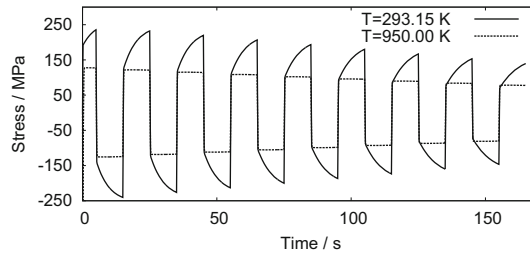


Fig. 11 Stress evolution for 8 cycles of a uniaxial strain-controlled tension–compression test for $T = 293.15$ K and $T = 950.00$ K

starts to evolve as soon as plastic deformation occurs. Furthermore, the parameters $S = 2.0$ MPa and $k = 0.5$ are used and assumed to be constant over temperature. In order to illustrate the stress softening predicted by the model with the aforementioned material parameters (see Table 4, 5), which will be used later on for the design studies, an uniaxial strain-controlled cyclic tension compression test is simulated. The test takes place at room temperature, and the strain cycle has an amplitude of $\epsilon = \pm 5\%$. The strain rate is about $\dot{\epsilon} = 0.01$ 1/s. Figure 11 shows the stress softening for $T = 293.15$ K and $T = 950.00$ K over 8 cycles (165 s).

Whenever possible, the material parameters should be identified on the basis of experimental data. To fully characterize the material parameters of the presented viscoplastic damage model, experimental tests including uniaxial tensile tests, creep and relaxation tests, cyclic tension–compression tests and damage tests for a wide temperature range have to be conducted. This testing programme is ongoing work. Nevertheless, the currently applied material parameters for the generic copper alloy are assumed to be sufficient to describe the behaviour of the fatigue specimen qualitatively and to identify critical geometries and boundary conditions. Certainly, the choice of the material parameters influences the simulation results quantitatively, but since the focus of this work is on qualitative studies, the chosen material parameters are expected to be sufficient.

4 Thermal boundary conditions

To approximate the thermal boundary conditions for the fatigue specimen, a one-dimensional conjugate heat transfer model is set up for the hot gas steady state. The resultant heat transfer coefficients and bulk temperatures on the hot gas and coolant side are used in the subsequent transient 2D thermal analyses, see Sect. 5.

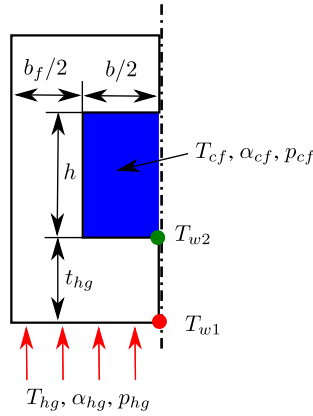


Fig. 12 Sketch of the cooling channel

Table 6 Combustion chamber and hot gas parameters

Chamber width	w_c	mm	48
Chamber height	h_c	mm	12
Chamber cross section area	A_c	mm ²	576
Equivalent chamber diameter	d_c	mm	27.1
Mixture ratio	O/F	–	3.5
Hot gas pressure	p_{hg}	MPa	2
Hot gas mass flow rate	\dot{m}_{hg}	kg/s	0.252
Hot gas specific heat capacity	$c_{p,hg}$	J/(kg K)	2157
Hot gas thermal conductivity	λ_{hg}	W/(m K)	0.244
Hot gas temperature	T_{hg}	K	3435
Hot gas wall temperature	T_{w1}	K	950
Hot gas heat flux	q_{hg}	MW/m ²	7.4

4.1 1D conjugate heat transfer model

The coupled heat transfer problem of the combustion chamber cooling channel structure is modelled by taking into account convection between the hot gas and the hot gas facing wall, the heat conduction inside the cooling channel structure and the convection between the structure and the cooling fluid. A sketch of the cooling channel geometry is shown in Fig. 12. The resulting stationary heat flux q of the heat transfer problem is determined by

$$q = \frac{T_{hg} - T_{cf}}{\frac{1}{\alpha_{hg}} + \frac{t_{hg}}{\lambda_s} + \frac{1}{\alpha_{cf,f}}}, \quad (19)$$

with the hot gas temperature T_{hg} , the cooling fluid temperature T_{cf} , the hot gas heat transfer coefficient α_{hg} , the hot gas wall thickness t_{hg} , the structural thermal conductivity λ_s and the cooling fluid heat transfer coefficient $\alpha_{cf,f}$. Here $\alpha_{cf,f}$ is a modified value of the cooling fluid heat transfer coefficient α_{cf} (see Eq. 22) taking into account the fin effect.

4.2 Hot gas convection

The combustion, resulting gas composition and gas properties are computed using the NASA software CEA2 of Gordon and McBride [32]. The design point for the fatigue specimen is chosen to be at a combustion chamber pressure of 2 MPa and a defined oxygen-to-fuel mixture ratio of 3.5. The relevant input parameters and results of the hot gas assumption can be taken from Table 6. A hot gas mass flow rate of $\dot{m}_{hg} = 0.252$ kg/s is necessary to reach the desired chamber pressure of 2 MPa. Outputs of computed chemical equilibrium composition are the hot gas temperature, the hot gas specific heat capacity and the hot gas thermal conductivity.

The heat release of the combustion processes is modelled as pure convection with a hot gas heat transfer coefficient α_{hg} based on a modified Nusselt correlation proposed by Cinjarew to be found in Kirchberger et al. [33]:

$$\alpha_{\text{hg}} = 0.01975 \frac{\lambda_{\text{hg}}^{0.18} (\dot{m}_{\text{hg}} c_{p,\text{hg}})^{0.82}}{d_c^{1.82}} \left(\frac{T_{\text{hg}}}{T_{w1}} \right)^{0.35} . \quad (20)$$

The variables are the hot gas thermal conductivity λ_{hg} , the hot gas mass flow rate \dot{m}_{hg} , the hot gas specific heat capacity $c_{p,\text{hg}}$, the diameter of a round chamber with equivalent cross section area d_c and the wall temperature facing the hot gas T_{w1} .

With the approximation of α_{hg} using Eq. 20, the heat flux q through the hot gas wall is

$$q_{\text{hg}} = \alpha_{\text{hg}} (T_{\text{hg}} - T_{w1}) . \quad (21)$$

Carlile and Quentmeyer [24] state that for the occurrence of the doghouse effect, the lower temperature bound for T_{w1} is between 700 K and 810 K. The maximum hot gas wall temperature $T_{w1} = 950$ K is selected as design point in order to promote an early failure after a small amount of engine cycles. During the experiment, the amount of load cycles to failure will be analysed by varying this temperature in the range of 800–950 K. The surface temperature T_{w1} can only be monitored indirectly because temperature is measured 1 mm away from the hot gas wall inside the cooling channel fin. The offset of the hot gas wall temperature needs to be estimated by evaluating the thermal gradient using measurements at different heights and by comparison with detailed finite element simulations.

For the design point of a hot gas wall temperature of $T_{w1} = 950$ K and a fixed combustion condition at $p_{\text{hg}} = 2$ MPa (for other parameters for the design point, see Table 6), the hot gas heat transfer coefficient can be determined by Eq. 20 to $\alpha_{\text{hg}} = 2.99$ kW/(m² K). The resulting hot gas heat flux is $q_{\text{hg}} = 7.4$ MW/m².

4.3 Cooling fluid convection

The cooling fluid convection can be estimated taking into account the cooling channel through the assumption of an open cooling fin. The cooling fluid heat transfer coefficient with fin effect is

$$\alpha_{\text{cf},f} = \alpha_{\text{cf}} \frac{b + \eta_{\text{fin}} 2h}{b + b_f} , \quad (22)$$

where α_{cf} denotes the cooling fluid heat transfer coefficient without fin effect, b is the cooling channel width, h is the cooling channel height, and b_f is the fin thickness. The fin efficiency η_{fin} is the ratio of the actual heat flow through the fin and the ideal heat flow with constant base temperature throughout the fin:

$$\eta_{\text{fin}} = \frac{\tanh \left(\sqrt{\frac{2\alpha_{\text{cf}} b_f}{\lambda_s} \frac{h}{b_f}} \right)}{\sqrt{\frac{2\alpha_{\text{cf}} b_f}{\lambda_s} \frac{h}{b_f}}} . \quad (23)$$

4.4 Iterative scheme

The hot gas heat flux determined by Eqs. 20 and 21 can be used as a fixed boundary condition, which has to be balanced ($q_{\text{hg}} = q$) by the cooling fluid heat transfer coefficient α_{cf} such that the desired hot gas wall temperature $T_{w1} = 950$ K is reached. For a defined cooling channel geometry and a defined structural material, the only unknown of Eqs. 19, 22 and 23 is α_{cf} . Because of the complexity of Eq. 23, α_{cf} has to be computed iteratively.

Using an initial guess for the cooling fluid heat transfer coefficient $\alpha_{\text{cf},0}$ in Eqs. 23 and 22, the initial heat flux q_0 can be computed with Eq. 19. The residual r is as follows:

$$r = q_{\text{hg}} - q_0 . \quad (24)$$

The heat flux residual $r(\alpha_{\text{cf}})$ is a function of the variable α_{cf} . The residual vanishes at the thermal equilibrium. The secant method is used to compute the coolant-side heat transfer coefficient α_{cf} until convergence is reached.

4.5 Cooling fluid estimation

A cooling fluid estimation is necessary in order to estimate a reasonable and realistic parameter space for the parameter variations analysed and discussed in Sect. 5.

Table 7 Parameter set for the conjugate heat transfer analyses

Hot gas wall thickness	t_{hg}	mm	1
Fin thickness	b_f	mm	2
Cooling channel width	b	mm	2.5
Cooling channel height	h	mm	8
Cooling channel fluid temperature	T_{cf}	K	293
Cooling channel fluid pressure	p_{cf}	MPa	7

The resultant heat transfer coefficient α_{cf} can be used to estimate the cooling fluid parameters through Nusselt correlations with the definition of the Nusselt number $Nu = (\alpha_{cf} d_h) / \lambda_{cf}$, where d_h is the hydraulic diameter and λ_{cf} is the cooling fluid heat conductivity. The Nusselt correlation Nu for a rectangular channel is taken from Meyer [34] and is defined as:

$$Nu = 0.023 Re^{0.8} Pr^{0.4} \left(\frac{T_{w2}}{T_{cf}} \right)^{-0.3}, \quad (25)$$

where Re and Pr are the Reynolds number and the Prandtl number, respectively. The cooling fluid temperature is denoted by T_{cf} . The cooling fluid facing wall temperature T_{w2} can be determined by $T_{w2} = T_{w1} - q t_{hg} / \lambda_s$. Solving Eq. 25 for Re , the necessary mass flow rate \dot{m}_{cf} of the cooling channel can be determined with

$$\dot{m}_{cf} = \frac{Re \mu_{cf}}{d_h} A_{cf}. \quad (26)$$

Here μ_{cf} denotes the dynamic viscosity of the cooling fluid and A_{cf} the cooling channel cross section. The thermodynamic fluid parameters of the cooling fluid such as μ_{cf} , λ_{cf} and $c_{p,cf}$ are evaluated through a bilinear interpolation of real gas tables depending on the cooling fluid pressure p_{cf} and the cooling fluid temperature T_{cf} . The real gas formulation and validation to generate these tables is published in Calvo and Hannemann [35].

The minimal mass flow rate of all cooling channels \dot{m}_a which is necessary to cool down the fatigue specimen for the fixed combustion chamber width is estimated by

$$\dot{m}_a = \dot{m}_{cf} \frac{w_c}{b + b_f}. \quad (27)$$

4.6 Cooling fluid analysis

In order to investigate the influence of geometric parameters as well as pressure and temperature on the mass flow rate \dot{m}_a (see Eq. 27), several parameter studies are conducted. For the following numerical results, a parameter set is defined, see Table 7. The analysed parameter variations deviate from this parameter set only for the studied and discussed parameter influence. From a designer point of view, these results have to be treated with care in order to formulate constraints which result from the nitrogen gas supply system. The nitrogen gas is provided through gas bundles at an initial pressure level of 30 MPa. Multiple engine cycles are requested with one set of gas bundles.

The influence of the fin effect on the conjugate heat transfer problem is analysed by the required mass flow rate of all channels and is shown in Fig. 13a. For the analysed fin thickness range between 1 mm and 5 mm, the mass flow rate \dot{m}_a varies between 418–445 g/s with a minimum at around 2 mm fin thickness. Using this fin thickness, a parameter variation of the cooling channel width b and height h has been analysed. In Fig. 13b, the contour lines show the mass flow rate \dot{m}_a for the cooling channel variation. The pressure valves and mass flow rate valves are designed to deliver a maximum of $\dot{m}_{max} = 1000$ g/s. Using a safety factor of 1.7, a limit of possible cooling channel variations for the subsequent 2D fatigue analyses in Sect. 5 can be identified with $\dot{m}_{max} = 588$ g/s.

Figure 14a, b shows the corresponding characteristic numbers Nu and Re of the cooling channel geometry variation in width and height as contour lines. A decrease in height results in an increasing Nusselt number Nu and Reynolds number Re . A larger impact on increasing Nu and Re is realised through a variation towards a larger cooling channel width.

Figure 15a shows the influence of the mass flow rate on the cooling fluid pressure. If the pressure is increased from 7 MPa to 15 MPa, a decrease in mass flow rate of around 10 % is observed. Compared to the

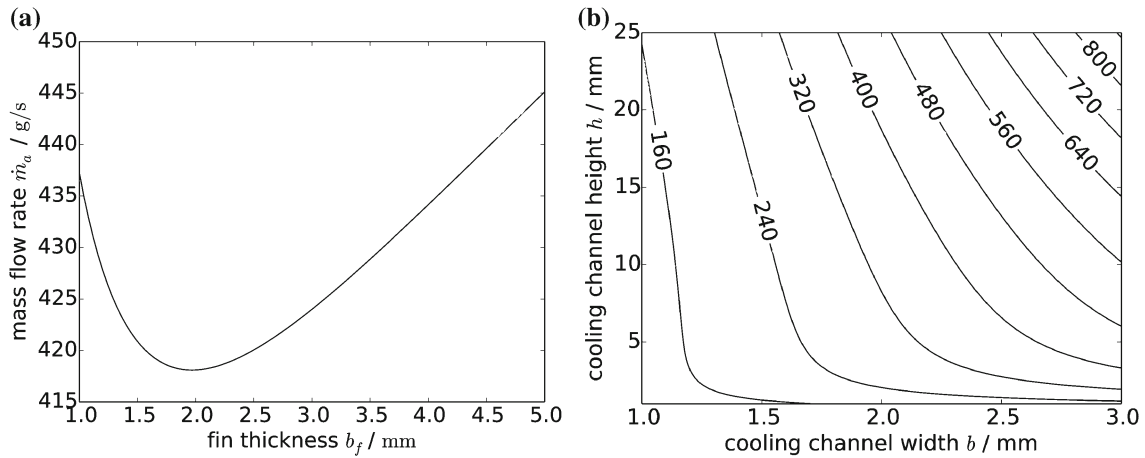


Fig. 13 Mass flow rate \dot{m}_a in dependency on the fin thickness and the cooling channel geometry. **a** Fin thickness variation. **b** Contour lines showing mass flow rate of all cooling channels \dot{m}_a in g/s

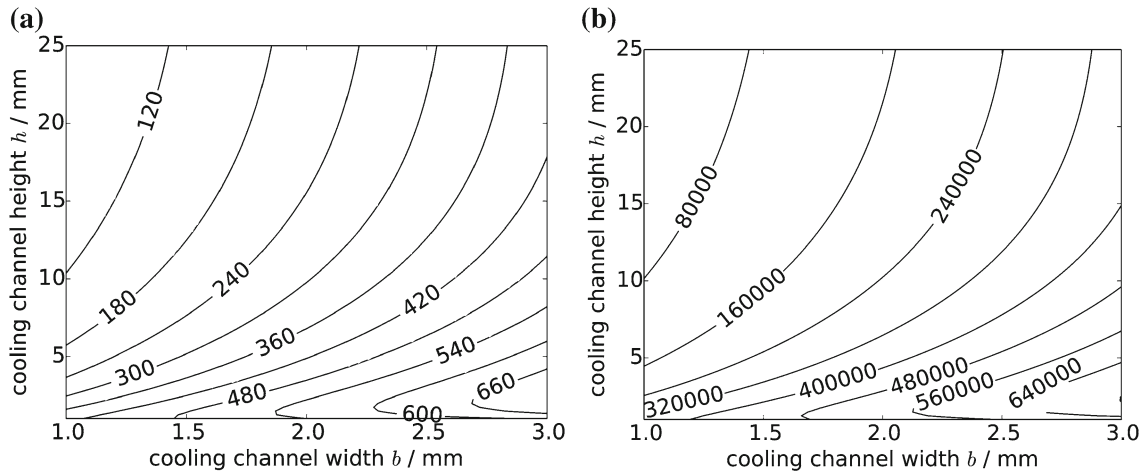


Fig. 14 Nusselt numbers Nu and Reynolds numbers Re in dependency on the cooling channel height and width. **a** Contour lines of the Nusselt number Nu . **b** Contour lines of the Reynolds number Re

available additional gas mass using a lower entrance pressure for the gas bundle blow-down, no advantage can be gained with a better cooling efficiency at higher pressures for the analysed pressure range.

Throughout an engine cycle, the cooling fluid entrance temperature cannot be kept constant. The temperature decreases because of the gas expansion inside the tank. In addition to this, the pressure regulation from 30 MPa to a pressure level of 7 MPa results in changing a temperature decrease because of the Joule–Thomson effect. In order to keep the hot gas wall temperature of 950 K at a constant level, a mass flow rate reduction of the cooling fluid would be necessary. The mass flow rate variation is shown in Fig. 15b for a cooling fluid temperature range between 243 and 303 K. The mass flow rate decrease is in the range of 6%. For the planned experiments, the mass flow rate is kept constant by a regulator. The entrance and exit cooling fluid temperature is measured for individual cooling channels. This interaction might be important for the validation of numerical coupling approaches and should be analysed during the experiment.

In reality, the estimated hot gas properties will vary and the estimated heat flux level can only be reached downstream of the injector head, where finalized combustion exists. Preliminary tests are planned to adjust the heat flux level by varying the mixture ratio at a constant pressure level. The position of the heat flux peak can be optimized for the specimen by changing the fatigue test segment position inside the modular combustion chamber.

The cooling system estimation depends on the validity of the given Nusselt correlation. For the planned experiments, the mass flow rate can be varied independently of the pressure level. Deviation from the estimation

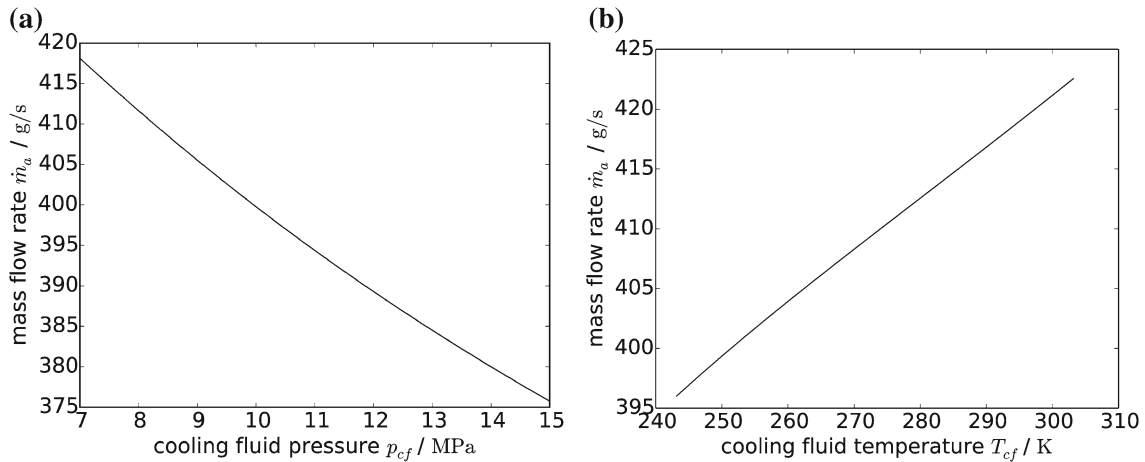


Fig. 15 Mass flow rate \dot{m}_a in dependence on the cooling fluid properties (pressure and temperature). **a** Pressure variation. **b** Temperature variation

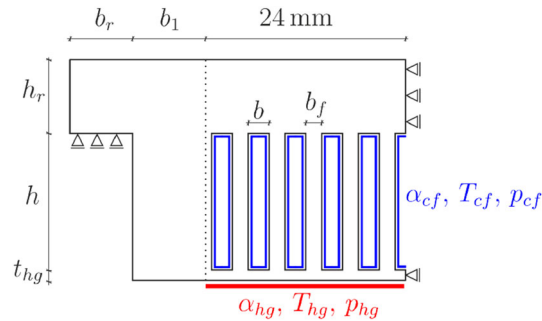


Fig. 16 Parametrized 2D cross section model

can be compensated by increasing or decreasing the mass flow rate of the coolant. This design feature is valuable to keep the specimen's hot gas wall temperature at the desired level without changing the mechanical loads acting on the structure.

5 Design studies for doghouse failure

In order to identify a suitable experimental set-up of the subscale rocket thrust chamber, several design studies have to be conducted. For these design studies, the procedure of sequentially coupled thermomechanical analysis is used. This means that the analysis is split into two parts. First, a transient thermal analysis is performed (see Sect. 5.1) to get the temperature field of the fatigue specimen in every time step. The computed temperature fields then serve as an input for a series of static analyses (see Sect. 5.2), in which the presented viscoplastic damage model (see Sect. 3) is applied. Preliminary studies based on one cycle (see Sect. 5.3) give insight into the influence of the geometry of the fatigue specimen on its qualitative deformation behaviour. Afterwards, studies based on multiple cycles (see Sect. 5.4) will help to identify critical boundary conditions as well as a suitable cooling channel configuration. Results concerning the variation of

- the geometry of the fatigue specimen,
- the thermal and mechanical boundary conditions and
- the cooling channel configuration

are presented in this section. For the following sensitivity analyses, the fatigue specimen shown in Fig. 8 is modelled via a parametrized 2D cross section of the half of the fatigue specimen exploiting symmetry conditions (cf. Fig. 16).

Table 8 Thermal material properties of the generic copper alloy

Properties	Generic copper alloy
Density ρ_s (kg/m ³)	9130
Thermal conductivity λ_s (W/mK)	310
Specific heat c_s (J/kg K)	373
Thermal expansion β_s (10 ⁻⁶ /K)	17.2

Table 9 Heat transfer coefficients and bulk temperatures in one cycle

Phase (-)	Time t (s)	Heat transfer coefficients		Bulk temperatures	
		α_{cf} (kW/m ² K)	α_{hg} (kW/m ² K)	T_{cf} (K)	T_{hg} (K)
Pre-cooling	0–2	≈1.8–5.0	–	293	–
Hot run	2–22	≈1.8–5.0	2.99	293	3435
Post-cooling	22–40	≈1.8–5.0	–	293	–

5.1 Transient thermal analysis

The general heat equation for transient problems without internal heat sources is given by

$$\Delta T = \frac{\rho_s c_s}{\lambda_s} \frac{\partial T}{\partial t} \quad (28)$$

with temperature T , time t and density ρ_s , specific heat c_s and the thermal conductivity λ_s of the structure (made out of a copper alloy). For the modelling of the cooling fluid and the hot gas, convective boundary conditions are defined (cf. Fig. 16):

$$\alpha_{cf} (T_{cf} - T) = \mathbf{n} \cdot \lambda \nabla T, \quad (29)$$

$$\alpha_{hg} (T_{hg} - T) = \mathbf{n} \cdot \lambda \nabla T, \quad (30)$$

where the involved parameters were already defined in Sect. 4.1. In Eq. 29, the temperature T represents the temperature on the surface of the cooling channels (e.g. T_{w2} in Fig. 12). In Eq. 30, the temperature T describes the temperature on the surface of the hot gas wall (e.g. T_{w1} in Fig. 12). For the free faces of the fatigue specimen, the derivation of the temperature T with respect to the normal direction of the boundary is assumed to be zero.

$$\frac{\partial T}{\partial \mathbf{n}} = \mathbf{0} \quad (31)$$

This implicates a perfect insulation of the fatigue specimen from the segment, which means that there is no heat transfer/flux between the specimen and the segment (adiabatic boundary condition). Finally, the initial condition of the whole fatigue specimen is given by

$$T(\mathbf{x}, t = 0) = 293 \text{ K}. \quad (32)$$

For the thermal material parameters of the fatigue specimen, the data for a generic copper alloy of Riccius and Zametaev [30] are used (see Table 8).

As mentioned already in Sect. 2.2, one operation cycle consists of 2 s pre-cooling, 20 s hot run and 18 s post-cooling. For the description of the thermal boundary conditions over time, see Table 9. The cooling fluid heat transfer coefficient α_{cf} is assumed to be constant over time, but is dependent on the cooling channel geometry (see Sect. 4). According to the iterative scheme, presented in Sect. 4.4, the coefficient α_{cf} is calculated for each cooling channel configuration and ranges approximately from 1.8 kW/(m² K) to 5.0 kW/(m² K). The bulk temperature of the coolant (nitrogen) is 293 K. The hot gas boundary condition is only active during the hot run. The bulk temperature of the hot gas T_{hg} is assumed to be 3435 K (cf. Table 6). The heat transfer coefficient α_{hg} reads 2.99 kW/(m² K), defined by Eq. 20 and the described design point (cf. Table 6). The bulk temperature T_{hg} and the heat transfer coefficient α_{hg} do not change abruptly from one time step to the next. They are supposed to linearly increase and decrease within 0.1 s. This assumption is on the safe side, because in reality this change is assumed to take longer. In order to model the very fast transition phases between the

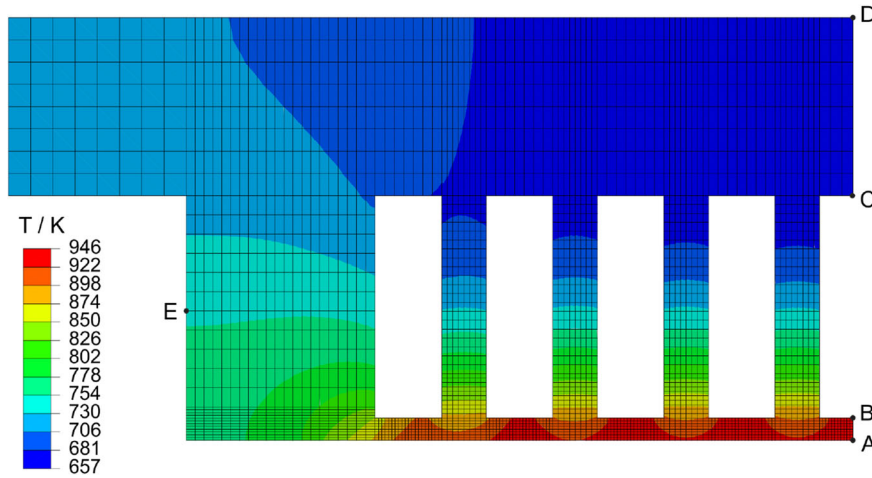


Fig. 17 Temperature distribution at the end of the hot run

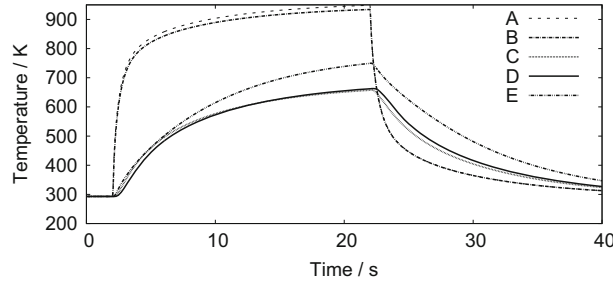


Fig. 18 Temperature over time for one cycle for the points A, B, C, D and E (see Fig. 17)

pre-cooling and the hot run as well as between the hot run and the post-cooling, individual time steps are prescribed. As an example for the thermal analyses, Fig. 17 shows the temperature distribution at the end of the hot run for a design with the following geometry: $h = 10 \text{ mm}$, $b = 3 \text{ mm}$, $b_f = 2 \text{ mm}$ and $t_{hg} = 1 \text{ mm}$ (cf. geometry parameters in Fig. 16). Figure 18 displays the corresponding temperature over time curves for the points A, B, C, D and E. The maximum temperature of about 947 K occurs, as expected, on the hot gas side in the symmetry line (point A). Point B reaches at the same time a temperature of about 932 K, which is 15 K lower. This generated temperature difference of 15 K is much lower than in the full-scale application (cf. Kowollik et al. [20]), since the heat load and the coolant power are lower for the subscale experiment. Additionally, in the case of a real rocket combustion chamber (see Fig. 1), the rear wall (nickel jacket) remains cool during the whole cycle, even during hot run. For the subscale experiment, no nickel jacket is used and the rear wall, represented by the points C and D, becomes relatively hot (up to 650 K). Another important area of the fatigue specimen is the side wall. The side wall should not become too hot, since the sealing on the side wall necessary to prevent entering hot gas into the gaps is highly sensitive to temperature. Point E, representing the side wall, reaches temperatures up to 750 K. This temperature would be much too high for the sealing, which is needed to ensure that the rectangular combustion chamber is tight. For this reason, the present design of the fatigue specimen cannot be realised and will be therefore modified as it is shown and explained in Sect. 5.4. Section 5.4 will additionally discuss the mechanical influences of a hot side wall. Figure 18 shows that at the end of the cycle almost ambient temperatures are reached at all points.

5.2 Quasi-static analysis

The temperature history obtained by the transient thermal analysis is now used for a series of static analyses. The general equation of balance of linear momentum is given by

$$\text{div}\sigma = \mathbf{0} \tag{33}$$

Table 10 Hot gas and coolant pressure applied for the static analyses

Phase (-)	Time t (s)	Hot gas pressure p_{hg} (MPa)	Coolant pressure p_c (MPa)
Pre-cooling	0–2	0	7
Hot run	2–22	2	7
Post-cooling	22–40	0	7

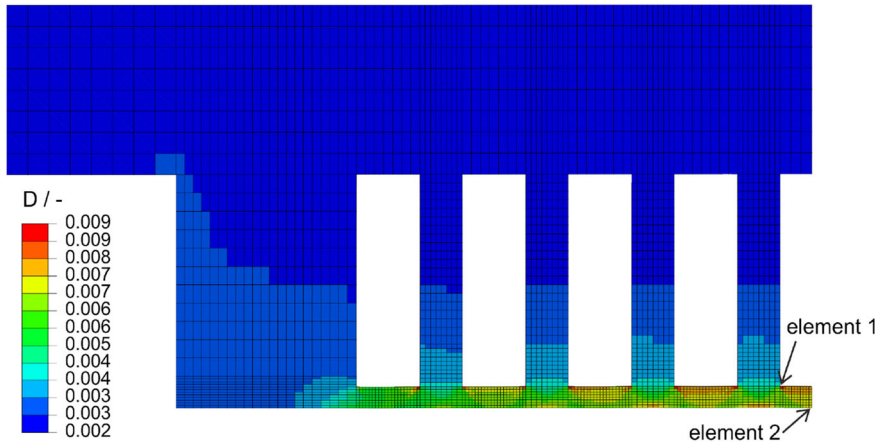


Fig. 19 Damage distribution after one cycle

and is solved in every time step. The temperature influence in the quasi-static analyses is considered by taking into account (i) the thermal strain (cf. Eq. 4) and (ii) the temperature dependence of the material parameters (cf. Table 4). For the finite element analysis, 8-node brick elements with reduced integration and hourglass stabilization are used. The boundary conditions for the half of the fatigue specimen are shown in Fig. 16. On the symmetry line, the displacements in horizontal direction are set to zero and the vertical fixture of the specimen is realised by a console with the width b_r and height h_r . All displacements in thickness direction are set to zero, leading to a plane strain condition. The pressure boundary conditions of the hot gas and the coolant are represented by the expression

$$t = \sigma n = \begin{pmatrix} t_n \\ t_t \\ t_z \end{pmatrix} = \begin{pmatrix} t_n \\ 0 \\ 0 \end{pmatrix}, \tag{34}$$

where the tangential component t_t and the z -component of the traction vector vanish. The normal component of the stress is equal to the pressure of the hot gas p_{hg} for the hot gas boundary condition and equal to the coolant pressure p_{cf} for the coolant boundary condition. The applied hot gas and coolant pressures for each phase of the cycle are listed in Table 10. Analogously to the heat transfer coefficients and bulk temperatures, the pressures are increased and decreased linearly during 0.1 s. As an example for the static analyses, the results of a one-cycle computation for a design with the geometry $h = 10$ mm, $b = 3$ mm, $b_f = 2$ mm and $t_{hg} = 1$ mm are discussed. Figure 19 shows the plot for the scalar damage variable D after one cycle. The same mesh as for the transient thermal analysis is used. Due to reduced integration, only one Gauss point per element is evaluated. In Fig. 19 and the following plots for D , the contour option is chosen in such a way that the value of D is displayed constantly over the element. This means that the value which is computed in the Gauss point is the one plotted for the whole element. The damage distribution in Fig. 19 shows that damage is mainly occurring in the hot gas wall. Maximum damage takes place at the corners of the cooling channels. In order to discuss the damage evolution during one cycle, Fig. 20 shows exemplarily the damage over time curves for elements 1 and 2, positioned at the centre channel. In both elements, qualitatively similar damage evolution is happening. For heating up ($t \approx 2$ s) as well as for cooling down ($t \approx 22$ s), damage increases abruptly. It can be seen that the simulation predicts more damage for cooling down than for heating up. Since during the cooling down phase the pressure difference between the coolant and the hot gas (7.0 MPa) is higher than during heating up (5.0 MPa), this is a reasonable result. The fact that damage increases mainly during the

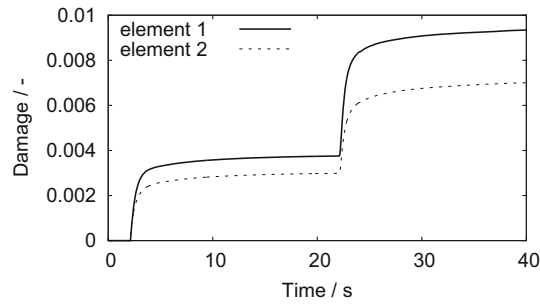


Fig. 20 Damage over time for one cycle for the elements 1 and 2 (see Fig. 19)

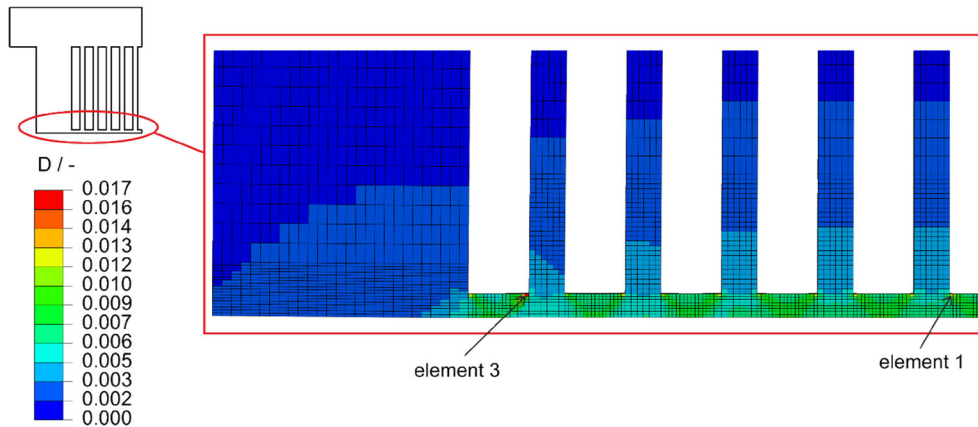


Fig. 21 Damage distribution after the first cycle for a cooling channel height of $h = 25$ mm

transient heating up and cooling down justifies the use of a short engine cycle with only 40 s. This allows to save fuel and coolant which are the main cost drivers.

5.3 Preliminary studies based on one cycle

In order to save computational time, the first computations have been performed for one cycle. The results of the following design studies allow us to identify general trends and will finally lead us to some important conclusions. For the studies based on one cycle, the focus is set on the geometry variation. The variation of the following geometry parameters is investigated (cf. Fig. 16):

- height of the cooling channels h ,
- width of the cooling channels b ,
- fin thickness b_f and
- rear wall thickness h_r .

Starting with a design of $b = 2.5$ mm, $b_f = 1.5$ mm, $t_{hg} = 1$ mm and $h_r = 12$ mm, three different cooling channel heights are investigated ($h = 10, 18$ and 25 mm). Figure 21 shows the damage distribution after one cycle for the design with the highest cooling channel ($h = 25$ mm, $h/b = 10$). For this high aspect ratio of the cooling channels, the maximum damage does not occur anymore at the centre channels, but in the one at the side (see element 3 in Fig. 21). However, this is not the desired position of maximum damage since we wish the failure of the structure to occur at the centre cooling channels, the place with the highest temperature. With increasing cooling channel height h , the side wall bending is intensified, leading to the undesired accumulation of damage in the side channel. Therefore, high cooling channels are not practical for the planned experiment. Another important factor is the cooling fluid consumption. The higher the cooling channels are, the more the cooling fluid is needed (cf. Fig. 13b). Figure 22 shows the influence of the cooling channel height h on the damage behaviour for element 1 and element 3, respectively. The damage evolution at the centre cooling channel is approximately the same for $h = 10$ mm and $h = 18$ mm (see Fig. 22a). For $h = 25$ mm, a

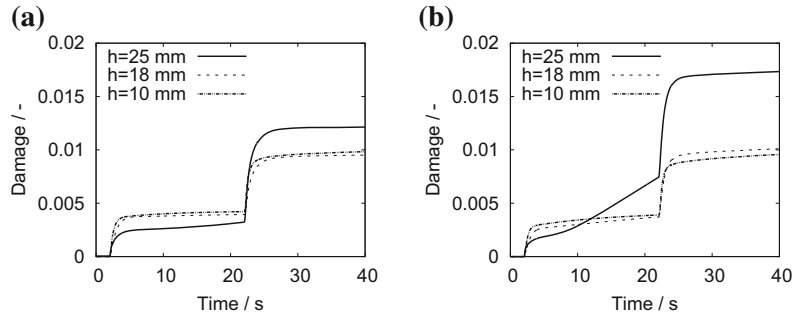


Fig. 22 Damage over time for one cycle for different cooling channel heights for elements 1 and 3 (see Fig. 21). **a** Element 1. **b** Element 3

Table 11 Influence of design parameters on the damage behaviour

Design parameter	Influence on damage	Remarks
Increasing cooling channel height h	Damage increases	Higher cooling channels do not lead to failure at the centre cooling channel; higher cooling channels require more coolant
Increasing cooling channel width b	Damage increases	Wider channels require more coolant
Increasing fin width b_f	Damage decreases slightly	Fin width is chosen according to a low mass flow rate of coolant (cf. Fig. 13a)
Increasing rear wall thickness h_r	Damage decreases	Thick rear wall generates a collet for the cooling channels, which guarantees mechanical boundary conditions for the specimen as independent of the fatigue segment as possible

different behaviour is observed. Indeed, the damage caused by heating up is smaller than for the other two heights, but the damage caused by cooling down is much higher so that at the end of the cycle the damage is about 25 % higher than for the other two heights. The damage at the side cooling channel (cf. Fig. 22b) is increasing with increasing cooling channel height. Comparing Fig. 22a with Fig. 22b reveals that for high cooling channels, damage in the side channel is higher than in the centre cooling channel. This is not desired due to the above-mentioned reason.

An overview of the results of the other parameter studies (variation of b , b_f and h_r) is shown in Table 11. For an increasing cooling channel width b , the damage in the fatigue specimen increases together with the doghouse deformation. However, wider channels require more cooling fluid (cf. Fig. 13b), so that a compromise between the mechanical and the economic point of view has to be found. For an increasing fin width b_f , the parameter studies reveal that the damage decreases slightly. Due to the negligible influence, the fin width can be chosen according to a low mass flow rate of coolant. Exploiting Fig. 13a, the optimized fin thickness is $b_f = 2.0$ mm. Finally, the influence of the rear wall thickness h_r is investigated. Here it shows up that damage decreases with increasing rear wall thicknesses. The aim for the specimen set-up is to generate mechanical boundary conditions for the specimen as independent of the fatigue segment as possible. This is crucial to be able to simplify validation models for the doghouse effect. Therefore, a comparably thick rear and side wall is preferred for the fatigue specimen. This approach generates a collet for the cooling channels by the specimen walls. In addition to this, small gaps are included between the fatigue specimen and the fatigue segment in order to decouple the mechanical boundary conditions as much as possible. Large gaps need to be avoided, otherwise, large amounts of hot gas enter the gaps and consequently heat up the sealing and fatigue segment.

5.4 Studies based on multiple cycles

Different cooling channel geometries with thick side and rear walls have been analysed for 20 thermomechanical cycles of the test sequence (2 s pre-cooling, 20 s hot run and 18 s post-cooling). Ensuring that maximum damage takes place at the centre cooling channels while limiting the consumption of fuel and coolant, the following geometry of the fatigue specimen is chosen: $h = 10$ mm, $b = 3$ mm, $b_f = 2$ mm and $t_{hg} = 1$ mm. For this geometry, the thermal boundary conditions are

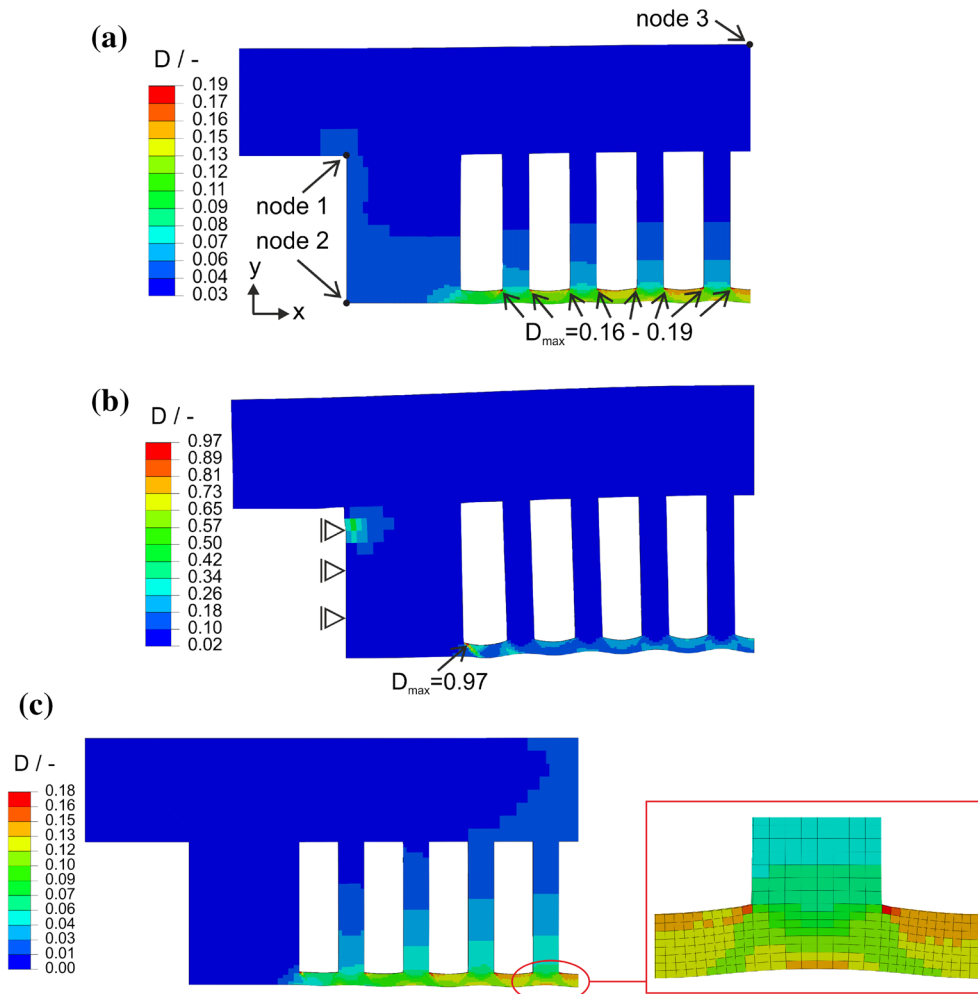


Fig. 23 Deformed contour plots of the damage parameter D after 20 cycles (deformation scale factor = 1). **a** Without side cooling, free side wall. **b** Without side cooling, additional boundary condition ($u_x = 0$ at the side wall). **c** With side cooling, free side wall

- $\alpha_{hg} = 2.99 \text{ kW}/(\text{m}^2 \text{ K})$, $T_{hg} = 3435 \text{ K}$ (calculated by Eq. 20),
- $\alpha_{cf} = 3.16 \text{ kW}/(\text{m}^2 \text{ K})$, $T_{cf} = 293 \text{ K}$ (calculated by the iterative scheme of Eq. 24).

The applied hot gas and coolant pressures are given in Table 10. Figure 23a shows the deformed structure and the distribution of the damage variable D after 20 cycles. Due to the chosen geometry, the maximum damage takes place in the corners of the centre channels. In this configuration, the thick side wall becomes too hot. Elevated temperatures in the range of 700 K during the hot run (cf. Fig. 17) result in large horizontal displacements of node 1 and node 2. Large gaps would be necessary to allow a free horizontal expansion of the structure. Moreover, node 3 experiences a vertical displacement if the side wall becomes that hot. If the horizontal displacement of the side wall is suppressed through an additional boundary condition, the maximum damage region is shifted to the side wall cooling channel interface, see Fig. 23b. As already mentioned before, maximum damage is desired at the point with the highest temperature (centre cooling channels), so that this additional boundary condition is not the method of choice.

To ensure that maximum damage takes place in the centre cooling channels as well as to avoid the unsatisfactory horizontal displacements of node 1 and node 2 as well as the vertical displacement of node 3, a configuration with an additional cooling on the side wall is tested. The additional side cooling is carried out with a heat transfer coefficient of $10 \text{ kW}/(\text{m}^2 \text{ K})$ and a bulk temperature of 293 K. As Fig. 23c shows, the additional cooling is able to satisfy the aforementioned requirements.

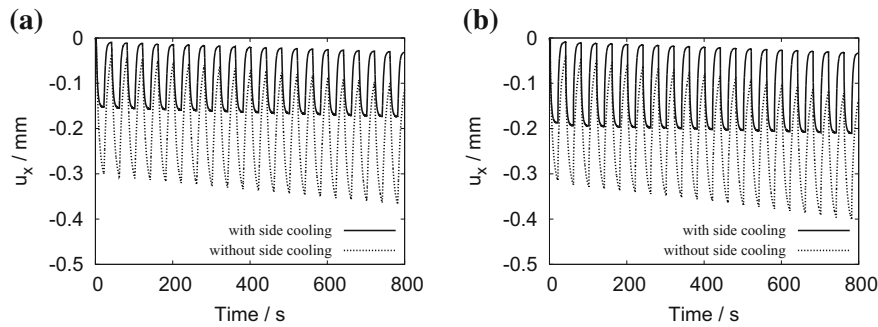


Fig. 24 Horizontal displacements of node 1 and node 2 (see Fig. 23a). **a** Node 1. **b** Node 2

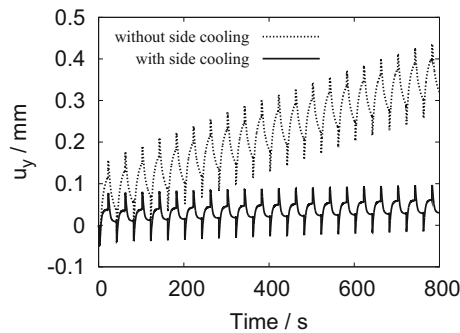


Fig. 25 Vertical displacements of node 3 (see Fig. 23a)

To demonstrate the improvements of the configuration with the side wall cooling quantitatively, the horizontal displacements of nodes 1 and 2 (cf. Fig. 23a) are analysed. Figure 24 shows the horizontal displacements over time for both nodes. For the fatigue specimen without side cooling, the displacements for both nodes are more than twice as large as for the fatigue specimen with side cooling. Additionally, for the latter configuration the maximum displacements are more or less constant over the number of cycles, whereas for the fatigue specimen without side cooling the maximum displacements increase over the cycles. During one cycle, the displacements are maximum at the beginning of the hot run, then decrease during the remaining hot run duration and become a minimum at the beginning of the cooling phase, before finally increasing again. Owing to the use of sealings, the absolute values of the horizontal displacements of both nodes are of interest. Without side cooling, the maximum absolute value of the displacements is about 0.4 mm, with side cooling the maximum value is only the half (0.2 mm). Thus, smaller gaps are needed for the construction with side cooling, which means that less hot gas enters the gaps.

Another aspect is the vertical displacement of the rear wall (represented by node 3). The higher the vertical displacement is, the more difficult the implementation of the flange gasket is. Figure 25 shows the vertical displacement of node 3 for both variants. At the end of the 20th cycle, the displacement for the variant without side cooling is four times larger. For extreme vertical movement of the rear wall, see Fig. 23b, for which the displacement of node 3 was not plotted. For the configuration with side cooling, the places of maximum damage concentrate at the centre cooling channels, as desired (see Fig. 23c). Furthermore, the typical bulging of the doghouse effect is present, which can be nicely seen in the zoomed illustration for the centre channels in Fig. 23c. The temperature profile of the configuration with additional cooling on the side wall is shown in Fig. 26 for the end of the hot run. The additional cooling has an influence on the hot gas wall temperature, which is about 50 K lower than for the initial configuration without side cooling. This can be compensated by reduced nitrogen cooling of the cooling channels. Figure 27 shows the transient temperature behaviour of the hot gas wall at the symmetry line. During the 20 s hot run, nearly a steady state is reached. The 18 s post-cooling is also sufficient to reach ambient conditions.

As a preliminary result, it can be summarized that a deformation of the cooling channels similar to the doghouse failure mode can be realised at lower heat loads with a flat fatigue specimen. For sealing, gap control and the flange gasket, a cooled side wall is necessary. Moreover, it could be shown that a cold rear wall is not essential for the typical deformation behaviour.

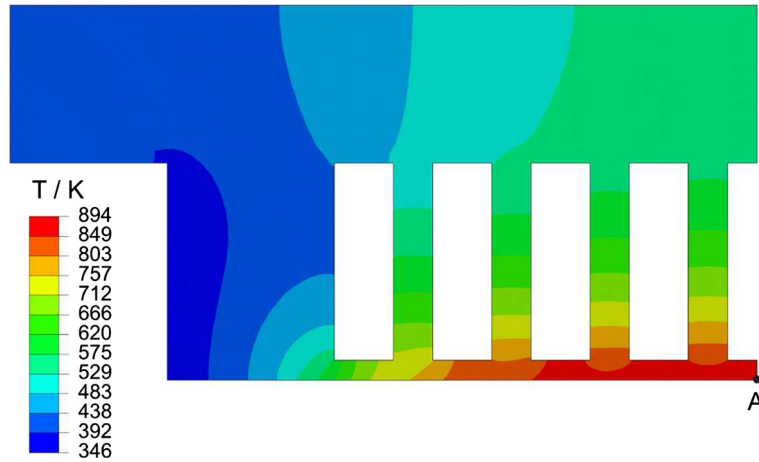


Fig. 26 Temperature profile at the end of the hot gas run for the additional side-cooled configuration

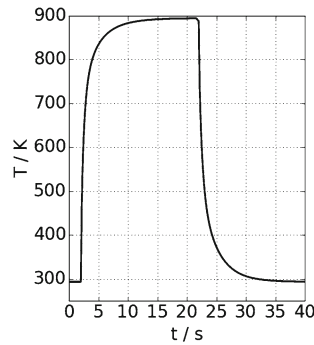


Fig. 27 Temperature over time of point A (see Fig. 26) for one cycle

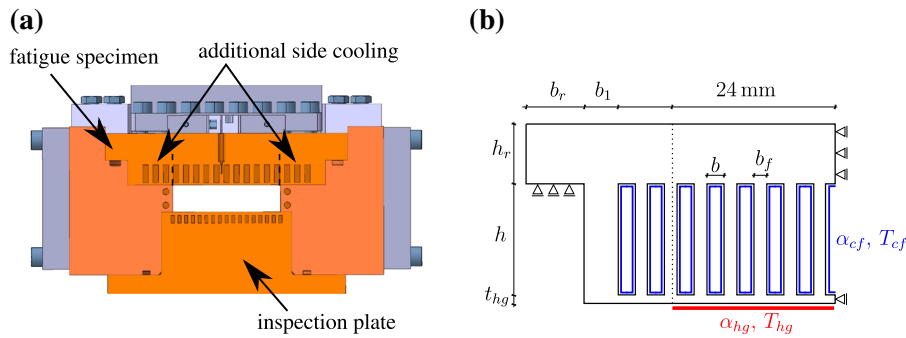


Fig. 28 Test segment with the installed fatigue specimen (additional cooling channels) and its parametrization. **a** Cross section view of the fatigue test segment with additional cooling channels beyond the hot gas interface. **b** Parametrized 2D cross section model with additional cooling channels

The following studies will focus on the side cooling of the fatigue specimen through additional cooling channels beyond the hot gas interface. Such a configuration is shown in Fig. 28a. The corresponding parametrized 2D cross section model is given in Fig. 28b. The number of the additional cooling channels in the side wall is dependent on the maximum desired side wall temperature. The more the additional cooling channels used are, the lower the temperature in the side wall becomes.

For the final studies, three additional cooling channels at each side are chosen, so that the fatigue specimen contains in total 17 cooling channels. The geometry parameters are set in the following way: $h = 8$ mm, $b = 2.5$ mm, $b_f = 2$ mm, $t_{hg} = 1$ mm, $h_r = 13$ mm, $b_1 = 6.5$ mm and $b_r = 8$ mm. Compared to the preceding configuration, the height h and the width b of the cooling channels are slightly decreased since the

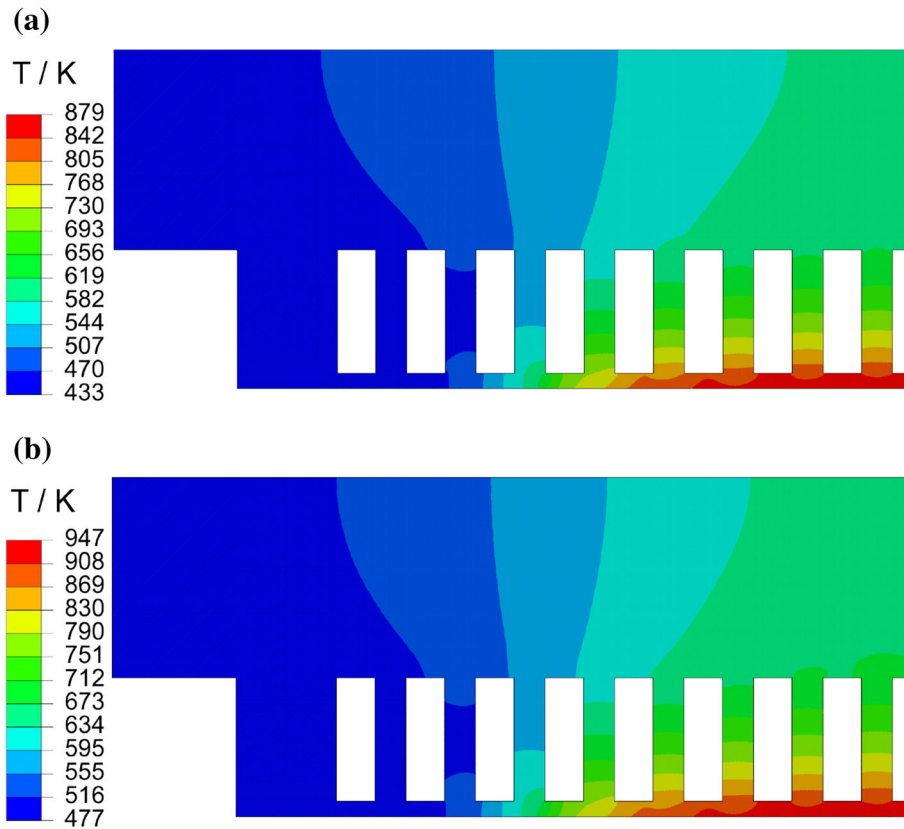


Fig. 29 Temperature distribution at the end of the hot run. **a** Heat transfer coefficient based on Sect. 4 ($\alpha_{cf} = 3.22 \text{ kW}/(\text{m}^2 \text{ K})$). **b** Reduced heat transfer coefficient ($\alpha_{cf} = 2.55 \text{ kW}/(\text{m}^2 \text{ K})$)

new configuration has more cooling channels which would have increased the mass flow rate of the cooling fluid. For three additional channels on each side, the maximum temperature of the side wall at the end of the hot run is about 450 K (see Fig. 29a). Compared to the design without side cooling (cf. Fig. 17), this is a reduction of over 350 K. In this first computation, a heat transfer coefficient of $\alpha_{cf} = 3.22 \text{ kW}/(\text{m}^2 \text{ K})$, calculated by the iterative scheme of Eq. 24, is used for all cooling channels, assuming a hot gas wall temperature of 950 K. As we can see in Fig. 29a, the desired hot gas wall temperature of 950 K is not reached ($T_{\max} = 879 \text{ K}$). This is reasonable, since the additional cooling channels are not considered by the approach used for the estimation of the thermal boundary conditions (see Sect. 4). To reach 950 K, the mass flow rate of the cooling channels (cf. Eq. 26) has to be reduced. This is obtained by just reducing the heat transfer coefficient. After some iterations, the heat transfer coefficient is found to read $\alpha_{cf} = 2.55 \text{ kW}/(\text{m}^2 \text{ K})$. The resulting temperature distribution for the reduced heat transfer coefficient at the end of the hot run is shown in Fig. 29b. The maximum temperature of $T_{\max} = 947 \text{ K}$, occurring at the centre channel on the hot gas side, shows that the desired hot gas wall temperature of approximately 950 K is now reached. On the other hand, the reduced heat transfer coefficient leads to an increase in the side wall temperature to 490 K. However, this is still a tremendous decrease compared to the version without side cooling.

After this thermal finite element analysis of the new channel configuration, the quasi-static analysis is performed in order to check the deformation and damage behaviour of the specimen. Figure 30 shows the damage distribution after 20 cycles for both variants. No bulging is observed for the side cooling channels due to the lower temperature there. Maximum damage is occurring at the corners of the centre cooling channel, as the zoomed illustrations highlight. Figure 31 shows the comparison of the damage evolution for the element with the maximum damage (at the corner of the centre cooling channel) for both variants. A higher maximum wall temperature ($\alpha_{cf} = 2.55 \text{ kW}/(\text{m}^2 \text{ K})$, $T_{\max} = 947 \text{ K}$) leads to larger damage than a lower maximum wall temperature ($\alpha_{cf} = 3.22 \text{ kW}/(\text{m}^2 \text{ K})$, $T_{\max} = 879 \text{ K}$). To quantitatively compare the bulging deflection of both variants, the displacement difference Δu_y of nodes F and A (cf. Fig. 30) is evaluated. Fig. 32 shows the evolution of Δu_y over the total time of 20 cycles. Similar to the damage, the bulging deflection is higher for the

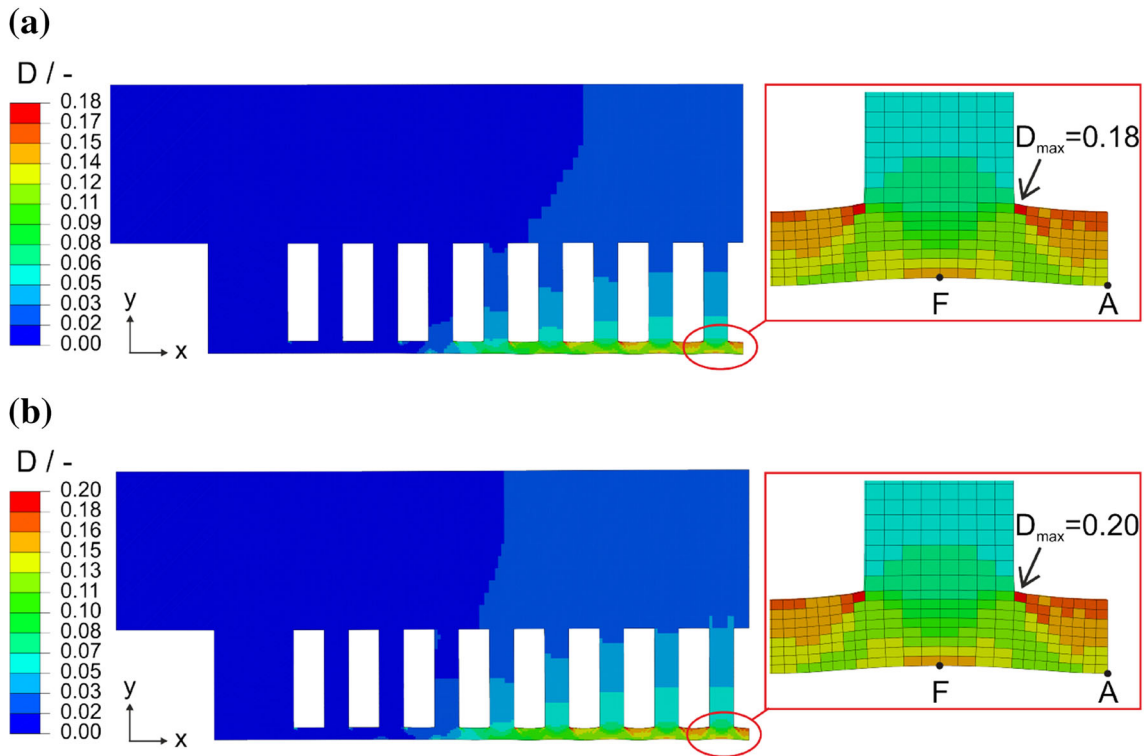


Fig. 30 Damage distribution after 20 cycles (deformed contour plot with deformation scale factor = 1). **a** Heat transfer coefficient based on Sect. 4 ($\alpha_{cf} = 3.22 \text{ kW}/(\text{m}^2 \text{ K})$, $T_{\max} = 879 \text{ K}$). **b** Reduced heat transfer coefficient ($\alpha_{cf} = 2.55 \text{ kW}/(\text{m}^2 \text{ K})$, $T_{\max} = 947 \text{ K}$)

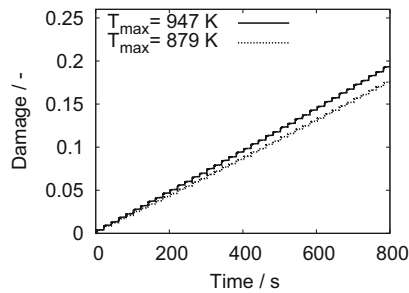


Fig. 31 Damage evolution at the corner of the centre cooling channel for different maximum temperatures

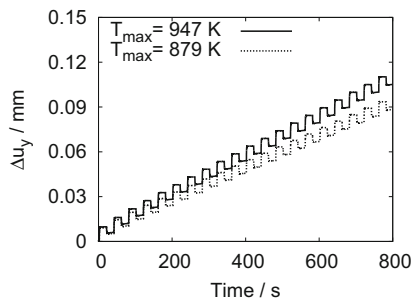


Fig. 32 Bulging deflection at the centre cooling channel for different maximum temperatures

higher maximum wall temperature, which is reasonable since the material softens with increasing temperature. In contrast to the damage evolution with two abrupt increases per cycle (also cf. Fig. 20), the bulging deflection

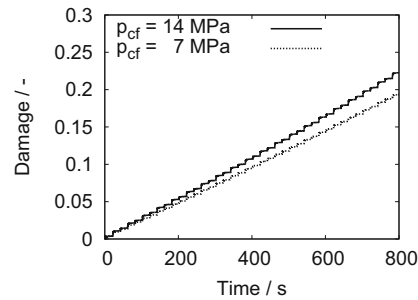


Fig. 33 Damage evolution at the corner of the centre cooling channel for different coolant pressures

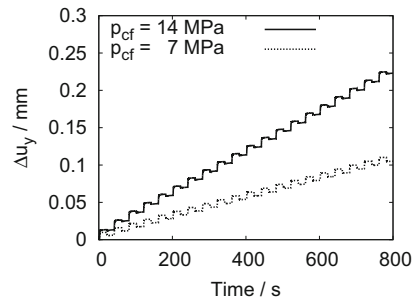


Fig. 34 Bulging deflection at the centre cooling channel for different coolant pressures

only increases significantly during the heating up phase. This is shown in Fig. 32 which displays only 20 steps in the progression of the curves.

As last point to be discussed, the influence of the coolant pressure p_{cf} on the damage and deformation behaviour of the fatigue specimen is investigated. So far, the coolant pressure has been set to $p_{cf} = 7$ MPa in order to meet the pressure difference between coolant and hot gas of the full-scale application. The coolant system of the subscale experiment is able to work up to $p_{cf} = 14$ MPa. In order to see the maximum influence of the coolant pressure, it is chosen to be $p_{cf} = 14$ MPa. Figure 33 shows that a higher coolant pressure leads to more damage accumulation. In addition, the bulging deflection is more than double for $p_{cf} = 14$ MPa (see Fig. 34). This means that besides the temperature level in the hot gas wall also the coolant pressure/pressure difference between coolant and hot gas has a noticeable influence on the deformation and the fatigue life.

As a result of the last studies, it can be furthermore concluded that also with additional cooling channels, a cooling channel deformation similar to the doghouse failure mode can be observed. The deformation of the hot gas wall of the fatigue specimen (see, for example, Fig. 30) is a little bit different from the one observed in the simulation for the full-scale application (see Kowollik et al. [20]). For the subscale fatigue specimen, the hot gas wall shows a more pronounced bulging towards the combustion chamber. One reason is the difference in the boundary conditions being present (full scale: rotational symmetry; subscale: two-dimensional). Another reason could be the much lower heat flux for the subscale experiment leading to a much lower temperature gradient in hot gas wall thickness direction. Nevertheless, the presented subscale experiment offers the possibility to validate the developed material model and the fluid–structure interaction environment presented in Kowollik et al. [20]. For sealing, gap control and the gasket, an optimized geometry of the fatigue specimen, optimized boundary conditions and an appropriate cooling channel configuration has been found. The cooling has to be reduced in order to reach the desired maximum hot gas wall temperature. Moreover, it has been demonstrated for one example that the bulging deflection and the damage are especially dependent on the maximum temperature occurring at the hot gas wall and the coolant pressure/pressure difference between coolant and hot gas.

6 Fatigue segment design outlook

The fatigue measurements are planned in two steps. The first step consists of the previously described fatigue segment with an actively cooled inspection plate, see Fig. 35a. The overcooled segment allows for long time test campaigns, where multiple fatigue specimens can be tested in order to generate a database for material failure

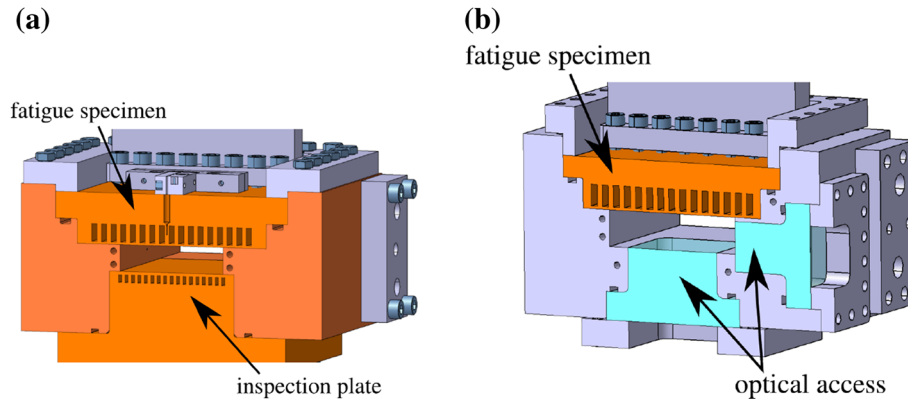


Fig. 35 Cut view of the two fatigue segments. **a** With dump-cooled inspection plate. **b** With two film-cooled optical access windows

and validation. In between the test cycles, the inspection plate will be dismounted and profile measurements of the fatigue specimen surface are planned in order to measure the growing cooling channel deformation response.

In a second step, a fatigue segment with extended measurements is planned. The idea is to measure the flow field in the vicinity of the centre channels of the fatigue specimen through particle image velocimetry (PIV) and to measure the deformation of these cooling channels throughout a test cycle. This is a novel and challenging approach for combustion chamber measurements. Two windows with film cooling will be integrated for the PIV measurements, see cut view in Fig. 35b. The window perpendicular to the fatigue specimen is needed for the PIV camera. The opposite window is large enough to place the necessary laser sheet at different locations of the specimen. In addition to this, a stereoscopic deformation measurement system will be applied through this optical access.

In addition to extended measurements, the experimental set-up will be used for a variety of specimens, e.g. with different cooling channel configurations, with thermal barrier coatings or made of ceramic material. Furthermore, an increased heat load is planned by raising the combustion pressure and by skewing the specimen.

7 Conclusions and outlook

In this work, design studies for the development of fatigue experiments of rocket engine cooling structures have been presented. A unified viscoplastic material model incorporating isotropic damage was utilized to identify a suitable experimental set-up for a rectangular subscale rocket thrust chamber. A design for a modular rectangular test chamber is presented. The main target of the experiment is to provide a database, which allows to validate several numerical approaches. Among these are coupling algorithms which take the hot gas, the structure and the cooling fluid into account. Another important issue is to model the material failure. In order to provide this database, the test chamber is carefully designed with respect to suitable boundary conditions of the specimen, measuring equipment, load case control and of course desired damage accumulation in the centre region of the specimen, where the highest temperatures occur. It is planned that the replaceable test specimen will be equipped with individual cooling channel mass flow rate control including temperature and pressure measurements at inlet and outlet to provide data for the cooling fluid analysis. The hot gas flow is monitored likewise at the inlet. Multiple thermocouples in the cooling channel fins are monitoring the temperature response during the cycles. Furthermore, the wall deformation and roughness increase can be measured in between cycles without influencing the specimen bearing. In the context of the damage accumulation, several important requirements were found during the design phase. It is crucial to define a cooling channel geometry which is prone to show the failure. Further, the bearing should not influence the desired damage position. Finally, additional side cooling is necessary to keep the sealing temperature low and to avoid large gaps.

The thermal boundary conditions of the fatigue specimen design have been approximated by an one-dimensional conjugate heat transfer model. Based on one-cycle computations as well as the limitation of fuel and cooling fluid consumption, a preliminary design was chosen. The studies based on multiple cycles considered the implementation of the flange gasket and gap control. The gaps could be minimized by an

additional side wall cooling. Finally, a configuration with additional cooling channels in the side wall has been proven to ensure this likewise. This set-up also exhibits the bulging of the cooling channel wall. In the end, a design satisfying the numerous requirements is suggested.

With the presented fatigue segment and its measuring equipment, a detailed investigation and analysis of the fluid–structure interaction phenomena occurring within combustion chambers is possible. Moreover, the structural response of the cooling channel wall can be studied and provides a basis for the validation of our recently developed damage models in combination with fluid–structure interaction. Besides the here-presented isotropic damage model, it is planned to apply also an anisotropic damage model including/excluding micro-defect closure effects.

A two-step approach is planned for the fatigue experiment. At first, the experiment is planned with a pure dump-cooled segment. If the fatigue specimen design proves to be suitable to generate a failure similar to the doghouse effect, a second fatigue segment with two windows and film cooling will be built in order to investigate the flow field and the deformation of the cooling channel structure throughout engine cycles.

Acknowledgments Financial support provided by the German Research Foundation (DFG) within the projects TPD3 and TPD9 of the CRC/Transregio 40 ‘Fundamental Technologies for the Development of Future Space-Transport-System Components under High Thermal and Mechanical Loads’ is gratefully acknowledged.

References

1. Quentmeyer, R.J.: Experimental fatigue life investigation of cylindrical thrust chambers. In: AIAA/SAE 13th Propulsion Conference (1977)
2. Riccius, R.J., Haidn, J.O., Zametaev, B.E. Influence of time dependent effects on the estimated life time of liquid rocket combustion chamber walls. In: 40th AIAA/ASME/SAE/ASEE Joint Propulsion Conference (2004)
3. Schwarz, W., Schwub, S., Quering, K., Wiedmann, D., Höppel, H.W., Göken, M.: Life prediction of thermally highly loaded components: modelling of the damage process of a rocket combustion chamber hot wall. *CEAS Space J.* **1**, 83–97 (2011). doi:[10.1007/s12567-011-0007-9](https://doi.org/10.1007/s12567-011-0007-9)
4. Dufailly, J., Lemaître, J.: Modeling very low cycle fatigue. *Int. J. Damage Mech.* **4**(2), 153–170 (1995). doi:[10.1177/105678959500400204](https://doi.org/10.1177/105678959500400204)
5. Fröhlich, A., Popp, M., Schmidt, G., Thelemann, D.: Heat transfer characteristics of H₂/O₂-combustion chambers. In: Joint Propulsion Conference and Exhibit, vol. 1 (1993)
6. Immich, H., Mayer, W.: Cryogenic liquid rocket engine technology developments within the german national technology programme. In: AIAA 97-2822, 33rd AIAA Joint Propulsion Conference (1997)
7. Anderson, W., Sisco, J., Sung, I.: Rocket combustor experiments and analyses. In: 14th Annual Thermal and Fluids Analysis Workshop (TFAWS) (2003)
8. Riccius, J.R., Bouajila, W., Zametaev, E.B.: Comparison of finite element analysis and experimental results of a combustion chamber type tmf panel test. In: 49th AIAA/ASME/SAE/ASEE Joint Propulsion Conference (2013)
9. Chaboche, J.L.: Constitutive equations for cyclic plasticity and cyclic viscoplasticity. *Int. J. Plast.* **5**(3), 247–302 (1989)
10. Chaboche, J.L.: On some modifications of kinematic hardening to improve the description of ratchetting effects. *Int. J. Plast.* **7**(7), 661–678 (1991)
11. Arya, V.K.: Application of finite-element-based solution technologies for viscoplastic structural analyses. *Commun. Appl. Numer. Methods* **7**, 435–444 (1991)
12. Arya, V.K., Arnold, S.M.: Viscoplastic analysis of an experimental cylindrical thrust chamber liner. *AIAA J.* **30**(3), 781–789 (1992)
13. DT Butler Jr., D.T., Aboudi, J., Pindera, M.J.: Role of the material constitutive model in simulating the reusable launch vehicle thrust cell liner response. *J. Aerosp. Eng.* **18**(1), 28–41 (2005). doi:[10.1061/\(ASCE\)0893-1321\(2005\)18:1\(28\)](https://doi.org/10.1061/(ASCE)0893-1321(2005)18:1(28))
14. Riccius, J.R., Hilsenbeck, M.R., Haidn, O.J.: Optimization of geometric parameters of cryogenic liquid rocket combustion chambers. In: AIAA 2001-3408, AIAA, pp. 1–11 (2001)
15. Riccius, J.R., Haidn, O.J., Zametaev, E.B.: Influence of time dependent effects on the estimated life time of liquid rocket combustion chamber walls. In: 40th AIAA/ASME/SAE/ASEE Joint Propulsion Conference and Exhibit (2004)
16. Riccius, J.R., Zametaev, E.B., Haidn, O.J., de Boisvilliers, G.: Comparison of 2D and 3D structural fe-analyses of lre combustion chamber walls. In: 42nd AIAA/ASME/SAE/ASEE Joint Propulsion Conference, AIAA (2006)
17. Schwarz, W., Wiedmann, D., Schwub, S., Höppel, H., Göken, M.: Assessment of different continuum damage models for life-time prediction of high thrust cryogenic combustion chambers. In: Proceedings of the 4th European Conference for Aerospace Sciences (EUCASS) (2011)
18. Perzyna, P.: The constitutive equations for rate sensitive plastic materials. *Q. Appl. Math.* **20**, 321–332 (1963)
19. Lemaître, J.: *A Course on Damage Mechanics*. Springer, Berlin (1992)
20. Kowollik, D., Tini, V., Reese, S., Haupt, M.: 3d fluid-structure interaction analysis of a typical liquid rocket engine cycle based on a novel viscoplastic damage model. *Int. J. Numer. Methods Eng.* **94**(13), 1165–1190 (2013)
21. Celano, M.P., Silvestri, S., Schlieben, G., Kirchberger, C., Haidn, O.J., Dawson, T., Ranjan, R., Menon, S.: Experimental and numerical investigation for a gox-gch₄ shear-coaxial injector element. In: Space Propulsion Conference 2014 (2014)
22. Astrium. Vulcain Rocket Engine—Thrust Chamber, January 2012. <http://cs.astrium.eads.net/sp/launcher-propulsion/rocket-engines/>

23. Kniesner, B., Frey, M., Knab, O.: Consideration of wall roughness effects in the prediction of heat transfer in rocket combustion chambers. In: European Conference for Aerospace Sciences, Munich (2013)
24. Carlile, J.A., Quentmeyer, R.J.: An Experimental Investigation of High-Aspect-Ratio Cooling Passages. National Aeronautics and Space Administration, Lewis Research Center, Cleveland (1992)
25. Frederick, C.O., Armstrong, P.J.: A mathematical representation of the multiaxial Bauschinger effect. *Mater. High Temp.* **24**, 1–26 (2007). doi:[10.3184/096034007X207589](https://doi.org/10.3184/096034007X207589)
26. Kachanov, L.M.: Time of the rupture process under creep conditions. *Isv. Akad. Nauk. SSR Otd. Tekh. Nauk.* **8**, 26–31 (1958). (in Russian)
27. Lion, A.: Constitutive modelling in finite thermoviscoplasticity: a physical approach based on nonlinear rheological models. *Int. J. Plast.* **16**(5), 469–494 (2000)
28. Voce, E.: The relationship between stress and strain for homogeneous deformation. *J. Inst. Metals* **74**, 537–562 (1948)
29. Thiede, R., Zametaev, E.B., Riccius, J.R., Fassin, M., Reese, S.: Comparison of damage parameter based finite element fatigue life analysis results to combustion chamber type tmf panel test results. In: 51st AIAA/SAE/ASEE Joint Propulsion Conference (2015)
30. Riccius, J.R., Zametaev, E.B.: Stationary and dynamic thermal analyses of cryogenic liquid rocket combustion chamber walls. 38th AIAA/ASME/SAE/ASEE Joint Propulsion Conference and Exhibit (2002)
31. Tini, V.: Lifetime prediction of a typical rocket combustion chamber by means of viscoplastic damage modeling. PhD Thesis, Rheinisch-Westfälische Technische Hochschule Aachen (2014)
32. Gordon, S., McBride, B.: Computer program for calculation of complex chemical equilibrium compositions and applications. Technical Report, NASA Reference Publication 1311 (1994)
33. Kirchberger, C., Wagnert, R., Kau, H., Soller, S., Martin, P., Bouchez, M., Bonzom, C.: Prediction and analysis of heat transfer in small rocket chambers. In: 46th AIAA Aerospace Science Meeting and Exhibit, AIAA 2008-1260 (2008)
34. Meyer, L.M.: The effect of cooling passage aspect ratio on curvature heat transfer enhancement. Technical Report, NASA Technical Memorandum 107426 (1997)
35. Calvo, J.B., Hannemann, K.: Numerical simulation of liquid rocket engine cooling channels. In: 45th AIAA/ASME/SAE/ASEE Joint Propulsion Conference & Exhibit, AIAA 2009-5302 (2009)